

A numerical model preserving nontrivial steady-state solutions for predicting waves run-up on coastal areas

Hasan Karjoun^a, Abdelaziz Beljadid^{a,b,*}

^a*Mohammed VI Polytechnic University, Green City, Morocco*

^b*University of Ottawa, Ottawa, Canada*

Abstract

In this study, a numerical model preserving a class of nontrivial steady-state solutions is proposed to predict waves propagation and waves run-up on coastal zones. The numerical model is based on the Saint-Venant system with source terms due to variable bottom topography and bed friction effects. The resulting nonlinear system is solved using a Godunov-type finite volume method on unstructured triangular grids. A special piecewise linear reconstruction of the solution is implemented with a correction technique to ensure the accuracy of the method and the positivity of the computed water depth. Efficient semi-implicit techniques for the friction terms and a well-balanced formulation for the bottom topography are used to exactly preserve stationary steady-state solutions. Moreover, we prove that the numerical scheme preserves a class of nontrivial steady-state solutions. To validate the proposed numerical model against experiments, we first demonstrate its ability to preserve nontrivial steady-state solutions and then we model several laboratory experiments for the prediction of waves run-up on sloping beaches. The numerical simulations are in good agreement with laboratory experiments which confirms the robustness and accuracy of the proposed numerical model in predicting waves propagation on coastal areas.

Keywords: Coastal areas; wave run-up/run-down; shallow water model; finite volume method; well-balanced discretization, positivity preserving property.

1. Introduction

Coastal areas involve several complex natural processes such as surface flows, sediment transport, soil erosion and moving shorelines. The propagation of waves on coastal areas near urban zones can have negative environmental impacts and cause considerable damages [1, 2, 3]. Understanding the dynamics of flow waves and predict its effects on coastal areas is necessary for developing solutions for sustainable water management and reducing water-related hazard including environment risks. Coastal wave propagation is mainly affected by the complex geometry of nearshore zones and the bottom topography. The rugged topography can cause many wave transformations such as wave refraction, diffraction, and breaking as the wave approaches the shoreline [4, 5, 6]. Wave run-up at the coastline is mainly depends on the offshore wave conditions such as height, length, and velocity

of waves and on the coastal geometry and topography [7]. Several previous studies have been devoted to predict waves propagation and determine the height of run-up along the coastlines [8, 9, 10, 11, 12, 13, 14, 15, 16, 17, 18]. Synolakis [19, 20] performed theoretical and experimental study to analyze the evolution of non-breaking and breaking solitary waves and approximated the wave maximum run-up, as well as the breaking criterion when the wave climbs up the sloping beach. Madsen and Mei [21] investigated the transformation of the solitary wave over an uneven bottom topography and showed that the wave height rises depending on the slope and its initial height. Kaplan [22] studied the evolution of periodic waves and derived an empirical formula for wave maximum run-up over a sloping beach.

The non-linear shallow water equations are among the commonly used models to describe the propagation of waves over variable bottom topography. These equations are derived from a depth-averaged integration of the 3D incompressible Navier–Stokes equations under the hydrostatic pressure assumption [23]. They are widely used for modeling water flows in lakes, rivers, and coastal areas [24, 25, 26, 27, 28, 29, 30]. Titov and Synolakis [31] tested the efficiency of the shallow water equations for modeling the evolution of breaking and non-breaking solitary waves on sloping beaches based on data from laboratory experiments. Delis et al. [13] developed a numerical model based on shallow water equations and investigated its accuracy to simulate long waves. Hu et al. [32] used nonlinear shallow water equations to perform numerical simulations of wave overtopping of coastal structures. Brocchini and Dodd [33] modeled nearshore flows using nonlinear shallow water equations and analyzed the interdependence between physical phenomena, model equations and numerical methods.

Various numerical methods have been developed for solving the shallow water equations modeling flows over variable bottom topography [34, 35, 36, 37, 38, 39]. The finite volume technique is one of the most popular tools used for solving the system of shallow water equations due to its capability to conserve mass and momentum, and accurately computes solutions with sharp gradients. Central-upwind finite volume methods are among the most efficient numerical tools developed for solving the system of conservation laws [40, 41]. The central-upwind schemes are Godunov-type free Riemann solver, which are based on the information obtained from the local speeds of wave propagation to approximate the numerical fluxes at the cell interfaces. Many extensions of these schemes have been proposed for the system of shallow water flow due to their robustness, high resolution and simplicity [42, 43, 44, 45, 25, 46, 47]. Furthermore, central-upwind schemes can be well-balanced and positivity preserving, that is, they accurately compute stationary steady solutions of the model and maintain the non-negativity of the computed water depth at the discrete level [48, 49, 50].

In this study, the depth-averaged 2-D shallow water equations are used for modeling waves propagation and waves run-up at the coastlines. The source terms due to variable bottom topography and bed friction effect are taken into account. The shallow water system is solved using an unstructured finite volume method based on central-upwind techniques [50, 41]. We used efficient semi-implicit techniques for the friction term and a well-balanced discretization for the source term due to variable topography. Beside the well-balanced property of the lack at rest, we established that the numerical scheme preserves nontrivial steady-state solutions over a slanted surface. Furthermore, a piecewise linear approximation

of the solution is implemented at the discrete level to ensure the accuracy of numerical scheme while guaranteeing the non-negativity of the computed water depth. Numerical simulations are performed to test the efficiency and the capability of the numerical model for predicting waves propagation and waves run-up on coastal areas.

The outline of this paper is as follows. We present the shallow water model with source terms due to variable bottom topography and bed friction effects in Section 2. The resulting nonlinear system of the shallow water flow model is solved using unstructured finite volume central-upwind technique on triangular meshes in Section 3. In Section 4, we perform numerical simulations to validate the proposed numerical model and test its capability for simulating waves propagation on coastlines. The numerical model is validated against laboratory experimental data and we perform numerical simulations to predict waves propagation along a sloping beach with complex bottom topography. Finally, some concluding remarks are provided in Section 5.

2. Governing equations

2.1. Shallow water equations

In this study, we consider the shallow water equations for modeling waves propagation and waves run-up on the coastal areas. Let $h(x, y, t)[m]$ be the water depth above the bottom topography $B(x, y)[m]$, and $\mathbf{u} = (u(x, y, t), v(x, y, t))^T[m/s]$ be the velocity field of the flow as shown in Figure 1. In a two-dimensional space, the shallow water equations with source terms due to variable bottom topography and bed friction effects can be written as follows:

$$\begin{cases} \partial_t h + \partial_x hu + \partial_y hv = 0, \\ \partial_t hu + \partial_x \left(hu^2 + \frac{g}{2} h^2 \right) + \partial_y (huv) = -gh\partial_x B - C_f u \sqrt{u^2 + v^2}, \\ \partial_t hv + \partial_x (huv) + \partial_y \left(hv^2 + \frac{g}{2} h^2 \right) = -gh\partial_y B - C_f v \sqrt{u^2 + v^2}, \end{cases} \quad (2.1)$$

where t represents the time, x and y are the cartesian coordinates and g is the gravity acceleration. The source terms in the momentum equations are the contributions of the bottom topography B and the friction terms $C_f u \sqrt{u^2 + v^2}$ and $C_f v \sqrt{u^2 + v^2}$, where the bed roughness coefficient C_f is computed using the Manning formula:

$$C_f = \frac{gn_f^2}{h^{1/3}}, \quad (2.2)$$

with n_f being the Manning coefficient which represents the bed hydraulic resistance to flow. The frictional resistance may have higher effects on flow velocity as the water depth decreases since the roughness coefficient C_f increases by decreasing the water depth [51].

The system of shallow water equations (2.1) can be expressed in the following matrix form:

$$\partial_t U + \partial_x F(U, B) + \partial_y G(U, B) = S(U, B) + M, \quad (2.3)$$

where we define new conservative variables $U := [w, q_x, q_y]^T$ of the system (2.1) and denote by $w := B + h$ the free-surface elevation and $q_x := uh$ and $q_y := vh$ the water discharges

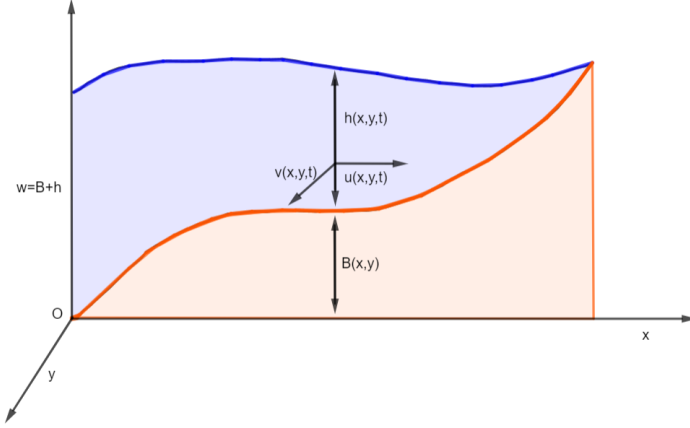


Figure 1: Schematic of the shallow water model variables on a coastal area.

along the coordinate directions Ox and Oy , respectively. The vectors of fluxes, bottom topography and friction term $(F, G)^T$, S and M respectively, are defined by:

$$\begin{aligned}
 F &:= \begin{bmatrix} q_x \\ \frac{q_x^2}{(w-B)} + \frac{g}{2}(w-B)^2 \\ \frac{q_x q_y}{(w-B)} \end{bmatrix}, \quad G := \begin{bmatrix} q_y \\ \frac{q_x q_y}{(w-B)} \\ \frac{q_y^2}{(w-B)} + \frac{g}{2}(w-B)^2 \end{bmatrix}, \\
 S &:= \begin{bmatrix} 0 \\ -g(w-B)\partial_x B \\ -g(w-B)\partial_y B \end{bmatrix}, \quad M := \begin{bmatrix} 0 \\ -\frac{gn_f^2}{h^{7/3}}q_x\sqrt{q_x^2+q_y^2} \\ -\frac{gn_f^2}{h^{7/3}}q_y\sqrt{q_x^2+q_y^2} \end{bmatrix},
 \end{aligned} \tag{2.4}$$

The Jacobian matrix of the shallow water system (2.3)-(2.4) has the following eigenvalues:

$$\boldsymbol{\lambda}_1 = un_x + vn_y - \sqrt{gh}, \quad \boldsymbol{\lambda}_2 = un_x + vn_y, \quad \boldsymbol{\lambda}_3 = un_x + vn_y + \sqrt{gh}, \tag{2.5}$$

which are used in the numerical scheme to compute the one-side local speeds of wave propagation, where $\boldsymbol{n} = [n_x, n_y]^T$ is the unit normal vector to the cell interfaces of control volumes used in our numerical methodology in Section 3.

2.2. Stationary steady-state solutions

The shallow water equations (2.1) with source terms is a system of balance laws. Under some particular initial conditions, this system has trivial steady-state solutions of the ‘‘lack at rest’’ ($\boldsymbol{u} = 0$) in the form:

$$q_x \equiv q_y \equiv 0, \quad \text{and} \quad w = h + B \equiv \text{constant}. \tag{2.6}$$

Furthermore, the shallow water system has a nontrivial steady-state solution which corresponds to the situation of steady flow with constant water depth and non-vanishing velocity over an inclined topography [49]:

$$\begin{aligned} h &= h_0 \equiv \text{constant}, q_x = q_0 \equiv \text{constant}, q_y \equiv 0, \partial_x B = -B_0 \equiv \text{constant}, \text{ and } \partial_y B \equiv 0, \text{ or} \\ h &= h_0 \equiv \text{constant}, q_x \equiv 0, q_y = q_0 \equiv \text{constant}, \partial_x B \equiv 0, \text{ and } \partial_y B = -B_0 \equiv \text{constant}. \end{aligned} \quad (2.7)$$

The expression of the water depth can be obtained by replacing the solution (2.7) in the momentum equations of the shallow water system (2.1).

$$h_0 = \left(\frac{n_f^2 q_0^2}{B_0} \right)^{3/10}. \quad (2.8)$$

The aforementioned trivial and nontrivial steady-state solutions (2.6)-(2.7) are used to test the proposed numerical model in terms of well-balanced and accuracy.

3. Numerical methodology

3.1. Numerical scheme

In this section, we briefly describe the finite volume central-upwind scheme on unstructured triangular grids applied to solve the system of shallow water equations (2.1) [50]. The computational domain is partitioned into triangular cells \mathbf{T}_j of size $|\mathbf{T}_j|$, and centers of mass $C_j := (\bar{x}_j, \bar{y}_j)$. We denote by $(\partial\mathbf{T}_j)_k$ the common interface of the cell \mathbf{T}_j and its neighboring cells \mathbf{T}_{jk} of length d_{jk} , $k = 1, 2, 3$. Let $\mathbf{n}_{jk} := (\cos(\theta_{jk}), \sin(\theta_{jk}))$ be the unit vector normal to $(\partial\mathbf{T}_j)_k$ pointed towards to the cell \mathbf{T}_{jk} , and (x_{jk}, y_{jk}) be the coordinates of the midpoint N_{jk} of the cell interface $(\partial\mathbf{T}_j)_k$ with corresponding vertices N_{jk_i} of coordinates (x_{jk_i}, y_{jk_i}) , $i = 1, 2$ as shown in Figure 2.

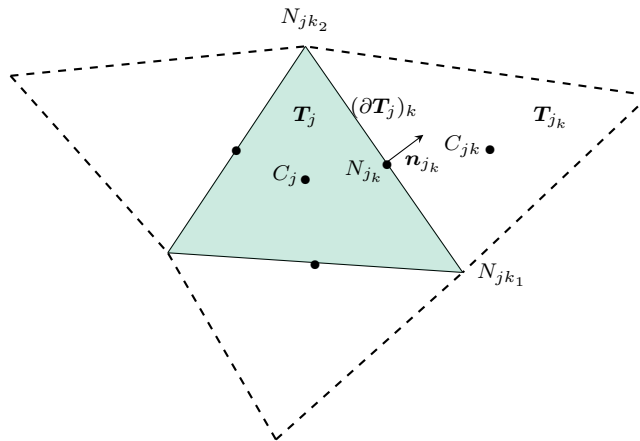


Figure 2: Schematic of triangular cells

We denote by \bar{U}_j the computed solution in the finite volume framework, and $\bar{\mathbf{S}}_j$ and $\bar{\mathbf{M}}_j$ the average values of the source terms over the cell \mathbf{T}_j , which are defined as follows:

$$\bar{U}_j(t) = \frac{1}{|\mathbf{T}_j|} \int_{\mathbf{T}_j} U(x, y, t) dx dy, \quad \bar{\mathbf{S}}_j(t) = \frac{1}{|\mathbf{T}_j|} \int_{\mathbf{T}_j} \mathbf{S}(x, y, t) dx dy, \quad \bar{\mathbf{M}}_j(t) = \frac{1}{|\mathbf{T}_j|} \int_{\mathbf{T}_j} \mathbf{M}(x, y, t) dx dy, \quad (3.1)$$

The central-upwind scheme on triangular meshes is applied to the system of shallow water equations (2.1)-(2.4), which is given by the following semi-discrete equation [50]:

$$\begin{aligned} \frac{\partial \bar{U}_j}{\partial t} = & - \frac{1}{|\mathbf{T}_j|} \sum_{k=1}^3 \frac{d_{jk} \cos(\theta_{jk})}{b_{jk}^{\text{in}} + b_{jk}^{\text{out}}} \left[b_{jk}^{\text{in}} F(U_{jk}(N_{jk}), B_{jk}) + b_{jk}^{\text{out}} F(U_j(N_{jk}), B_{jk}) \right] \\ & - \frac{1}{|\mathbf{T}_j|} \sum_{k=1}^3 \frac{d_{jk} \sin(\theta_{jk})}{b_{jk}^{\text{in}} + b_{jk}^{\text{out}}} \left[b_{jk}^{\text{in}} G(U_{jk}(N_{jk}), B_{jk}) + b_{jk}^{\text{out}} G(U_j(N_{jk}), B_{jk}) \right] \\ & + \frac{1}{|\mathbf{T}_j|} \sum_{k=1}^3 \frac{d_{jk} b_{jk}^{\text{in}} b_{jk}^{\text{out}}}{b_{jk}^{\text{in}} + b_{jk}^{\text{out}}} \left[U_{jk}(N_{jk}) - U_j(N_{jk}) \right] + \bar{\mathbf{S}}_j + \bar{\mathbf{M}}_j. \end{aligned} \quad (3.2)$$

In the numerical scheme (3.2), $U_j(N_{jk})$ and $U_{jk}(N_{jk})$ are respectively the reconstructed values of the solution at the left and right of cell interfaces $(\partial \mathbf{T}_j)_k$, computed at the midpoint N_{jk} and B_{jk} are the corresponding reconstructed values of the bottom topography B . The values b_{jk}^{in} and b_{jk}^{out} are the one side-local speeds of wave propagation computed using the small and large eigenvalues λ_1 and λ_3 of the Jacobian matrix of the shallow water system, given in Eq. (2.5) [50, 41],

$$\begin{aligned} b_{jk}^{\text{in}} &= - \min \left\{ \lambda_j^\theta - \sqrt{gh_j(N_{jk})}, \lambda_{jk}^\theta - \sqrt{gh_{jk}(N_{jk})}, 0 \right\}, \\ b_{jk}^{\text{out}} &= \max \left\{ \lambda_j^\theta + \sqrt{gh_j(N_{jk})}, \lambda_{jk}^\theta + \sqrt{gh_{jk}(N_{jk})}, 0 \right\}, \end{aligned} \quad (3.3)$$

where

$$\begin{aligned} \lambda_{jk}^\theta &:= \cos(\theta_{jk}) u_{jk}(N_{jk}) + \sin(\theta_{jk}) v_{jk}(N_{jk}), \\ \lambda_j^\theta &:= \cos(\theta_{jk}) u_j(N_{jk}) + \sin(\theta_{jk}) v_j(N_{jk}). \end{aligned} \quad (3.4)$$

The reconstructed values of the velocity at the cell interfaces, \mathbf{u}_j and \mathbf{u}_{jk} are computed using the following desingularization formula to prevent division by small computed values of water depth, where we omit the indices j and jk [52]

$$\mathbf{u} = \begin{cases} \frac{1}{h} \times \begin{bmatrix} q_x \\ q_y \end{bmatrix}, & \text{if } h \geq \eta, \\ \frac{\sqrt{2}h}{\sqrt{h^4 + \max\{h^4, \epsilon\}}} \times \begin{bmatrix} q_x \\ q_y \end{bmatrix}, & \text{if } h < \eta, \end{cases} \quad (3.5)$$

where the prescribed tolerances $\epsilon = \max_j \{|\mathbf{T}_j|^2\}$ and $\eta = 10^{-6}$ are used in our numerical simulations.

3.2. Linear reconstructions

In this section, we define the reconstructions of the bottom topography B and the conservative variables U of the system. The bottom topography is known at the cell vertices N_{jk_i} , since we use a linear reconstruction over the cell \mathbf{T}_j its values at the midpoint N_{jk} are obtained using the following linear approximation [50, 43]:

$$B_{jk} = \frac{B_{jk_1} + B_{jk_2}}{2}. \quad (3.6)$$

Similarly, the values of the topography \mathbf{B}_j at the center of mass C_j are computed as follows:

$$\mathbf{B}_j = \frac{1}{|\mathbf{T}_j|} \int_{\mathbf{T}_j} B(x, y) dx dy = \frac{B_{j1} + B_{j2} + B_{j3}}{3}. \quad (3.7)$$

To design the second-order numerical model, the values of vector variables at the midpoints of cell interfaces, $U_j(N_{jk})$ and $U_{jk}(N_{jk})$ are computed using the following piecewise linear reconstruction:

$$U_j(x, y) := \bar{\mathbf{U}}_j + (\partial \mathbf{U}_j)_x(x - \bar{x}_j) + (\partial \mathbf{U}_j)_y(y - \bar{y}_j), \quad (3.8)$$

where $(\partial \mathbf{U}_j)_x$ and $(\partial \mathbf{U}_j)_y$ are the two components of the numerical gradient of the vector U at the cell \mathbf{T}_j , computed following the approach developed in [53]:

$$\begin{aligned} (\partial \mathbf{U}_j^{(i)})_x &= \mathcal{W}_{j1}^{(i)} (\partial \mathbf{u}_{j1}^{(i)})_x + \mathcal{W}_{j2}^{(i)} (\partial \mathbf{u}_{j2}^{(i)})_x + \mathcal{W}_{j3}^{(i)} (\partial \mathbf{u}_{j3}^{(i)})_x, \\ (\partial \mathbf{U}_j^{(i)})_y &= \mathcal{W}_{j1}^{(i)} (\partial \mathbf{u}_{j1}^{(i)})_y + \mathcal{W}_{j2}^{(i)} (\partial \mathbf{u}_{j2}^{(i)})_y + \mathcal{W}_{j3}^{(i)} (\partial \mathbf{u}_{j3}^{(i)})_y, \text{ for } i = 1, 2, 3, \end{aligned} \quad (3.9)$$

where the initial gradients $(\partial \mathbf{u}_j^{(i)})_x$ and $(\partial \mathbf{u}_j^{(i)})_y$ at the cell \mathbf{T}_j are computed by constructing the plane passing through the centers of mass of three neighboring cells, $(\bar{x}_{j1}, \bar{y}_{j1}, \bar{\mathbf{U}}_{j1}^{(i)})$, $(\bar{x}_{j2}, \bar{y}_{j2}, \bar{\mathbf{U}}_{j2}^{(i)})$, and $(\bar{x}_{j3}, \bar{y}_{j3}, \bar{\mathbf{U}}_{j3}^{(i)})$ for i th component of the vector U , $i = 1, 2, 3$.

$$\begin{aligned} (\partial \mathbf{u}_j^{(i)})_x &= \frac{(\bar{y}_{j3} - \bar{y}_{j1})(\bar{\mathbf{U}}_{j2}^{(i)} - \bar{\mathbf{U}}_{j1}^{(i)}) - (\bar{y}_{j2} - \bar{y}_{j1})(\bar{\mathbf{U}}_{j3}^{(i)} - \bar{\mathbf{U}}_{j1}^{(i)})}{(\bar{y}_{j3} - \bar{y}_{j1})(\bar{x}_{j2} - \bar{x}_{j1}) - (\bar{y}_{j2} - \bar{y}_{j1})(\bar{x}_{j3} - \bar{x}_{j1})}, \\ (\partial \mathbf{u}_j^{(i)})_y &= \frac{(\bar{x}_{j2} - \bar{x}_{j1})(\bar{\mathbf{U}}_{j3}^{(i)} - \bar{\mathbf{U}}_{j1}^{(i)}) - (\bar{x}_{j3} - \bar{x}_{j1})(\bar{\mathbf{U}}_{j2}^{(i)} - \bar{\mathbf{U}}_{j1}^{(i)})}{(\bar{x}_{j2} - \bar{x}_{j1})(\bar{y}_{j3} - \bar{y}_{j1}) - (\bar{x}_{j3} - \bar{x}_{j1})(\bar{y}_{j2} - \bar{y}_{j1})}. \end{aligned} \quad (3.10)$$

The weights $\mathcal{W}_{j1}^{(i)}$, $\mathcal{W}_{j2}^{(i)}$, and $\mathcal{W}_{j3}^{(i)}$ are given by [53]:

$$\begin{aligned} \mathcal{W}_{j1}^{(i)} &= \frac{\|\partial \mathbf{u}_{j3}^{(i)}\|_2^2 \|\partial \mathbf{u}_{j2}^{(i)}\|_2^2 + \xi^2}{\|\partial \mathbf{u}_{j1}^{(i)}\|_2^4 + \|\partial \mathbf{u}_{j2}^{(i)}\|_2^4 + \|\partial \mathbf{u}_{j3}^{(i)}\|_2^4 + 3\xi^2}, \\ \mathcal{W}_{j2}^{(i)} &= \frac{\|\partial \mathbf{u}_{j3}^{(i)}\|_2^2 \|\partial \mathbf{u}_{j1}^{(i)}\|_2^2 + \xi^2}{\|\partial \mathbf{u}_{j1}^{(i)}\|_2^4 + \|\partial \mathbf{u}_{j2}^{(i)}\|_2^4 + \|\partial \mathbf{u}_{j3}^{(i)}\|_2^4 + 3\xi^2}, \\ \mathcal{W}_{j3}^{(i)} &= \frac{\|\partial \mathbf{u}_{j1}^{(i)}\|_2^2 \|\partial \mathbf{u}_{j2}^{(i)}\|_2^2 + \xi^2}{\|\partial \mathbf{u}_{j1}^{(i)}\|_2^4 + \|\partial \mathbf{u}_{j2}^{(i)}\|_2^4 + \|\partial \mathbf{u}_{j3}^{(i)}\|_2^4 + 3\xi^2}, \end{aligned} \quad (3.11)$$

where $\xi = 10^{-7}$ is considered to avoid division by zero.

3.3. Positivity reconstruction of the water depth

In this section, we will correct the linear reconstruction (3.8) for the free-surface elevation variable w to ensure the non-negativity of the reconstructed values h_j and h_{jk} of the water depth. Indeed, the correction technique is applied for triangles where we have $w_j(x_{jk_1}, y_{jk_1}) < B_{jk_1}$ in some vertices. Following the methodology developed by Bryson et al. [50] there are two cases where the correction technique is needed. The first case is where we have $w_j(x_{jk_1}, y_{jk_1}) < B_{jk_1}$ and $w_j(x_{jk_2}, y_{jk_2}) < B_{jk_2}$ at the cell interface $\partial(\mathbf{T}_j)_k$ and the second case is where only one vertex for which $w_j(x_{jk_1}, y_{jk_1}) < B_{jk_1}$. We set $w_{jk_1}^{corr} = B_{jk_1}$ at the vertices for which $w_j(x_{jk_1}, y_{jk_1}) < B_{jk_1}$ and for the rest of the vertices we use $w_{jk_1}^{corr} = \tilde{h}_j + B_{jk_1}$, where \tilde{h}_j is computed using the conservation requirement:

$$\tilde{h}_j = \frac{3\bar{h}_j}{\sum_{k=1}^3 \beta_k}, \text{ with } \beta_k = \begin{cases} 1, & \text{if } w_{jk_1} \geq B_{jk_1}, \\ 0, & \text{if } w_{jk_1} < B_{jk_1}, \end{cases} \quad (3.12)$$

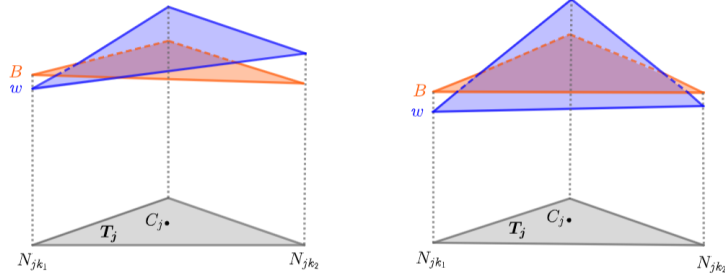


Figure 3: Schematic of the two cases where a correction procedure is applied: case 1 (right) and case 2 (left).

The corrected reconstruction h_j^{corr} for the water depth is conservative over the cell \mathbf{T}_j . Indeed, denote by \mathcal{V}^- and \mathcal{V}^+ the sets of vertices N_{jk_1} for which $w_j(x_{jk_1}, y_{jk_1}) < B_{jk_1}$ and $w_j(x_{jk_1}, y_{jk_1}) \geq B_{jk_1}$ of cardinals n^- and n^+ , respectively. Using the linear approximation we have:

$$\begin{aligned} \bar{h}_j^{corr} &= \frac{1}{|\mathbf{T}_j|} \int_{\mathbf{T}_j} h_j^{corr}(x, y) dx dy = \frac{1}{|\mathbf{T}_j|} \int_{\mathbf{T}_j} [w_j^{corr}(x, y) - B(x, y)] dx dy, \\ &= \frac{1}{3} \sum_{k=1}^3 [w_{jk_1}^{corr} - B_{jk_1}], \end{aligned} \quad (3.13)$$

where we use the values at the cell vertices N_{jk_1}

$$\begin{aligned} \bar{h}_j^{corr} &= \frac{1}{3} \sum_{N_{jk_1} \in \mathcal{V}^-} [w_{jk_1}^{corr} - B_{jk_1}] + \frac{1}{3} \sum_{N_{jk_1} \in \mathcal{V}^+} [w_{jk_1}^{corr} - B_{jk_1}], \\ &= \frac{1}{3} \sum_{N_{jk_1} \in \mathcal{V}^-} h_{jk_1}^{corr} + \frac{1}{3} \sum_{N_{jk_1} \in \mathcal{V}^+} h_{jk_1}^{corr}. \end{aligned} \quad (3.14)$$

Since $h_{jk_1}^{corr} = 0$ in \mathcal{V}^- and $h_{jk_1}^{corr} = \tilde{h}_j$ in \mathcal{V}^+ , then

$$\bar{h}_j^{corr} = \frac{1}{3} \sum_{N_{jk_1} \in \mathcal{V}^+} h_{jk_1}^{corr} = \frac{1}{3} n^+ \tilde{h}_j = \frac{1}{3} n^+ \frac{3\bar{h}_j}{\sum_{k=1}^3 \beta_k} = \bar{h}_j. \quad (3.15)$$

3.4. Discretization of the source terms

A suitable discretization of the bottom topography source term should be used to satisfy the well-balanced property of the numerical model in which the steady-state solutions (2.6)-(2.7) are preserved. In our study, we use the approach developed in [50] where the discretization of the topography source term balances the numerical fluxes. The well-balanced quadrature for the non-vanishing components of $\bar{\mathbf{S}}_j$ are:

$$\begin{aligned} \bar{\mathbf{S}}_j^{(2)} &= \frac{1}{2|\mathbf{T}_j|} \sum_{k=1}^3 g d_{jk} [B_{jk} - w_j(N_{jk})]^2 \cos(\theta_{jk}) + g(\partial \mathbf{w}_j)_x [\mathbf{B}_j - \bar{\mathbf{w}}_j], \\ \bar{\mathbf{S}}_j^{(3)} &= \frac{1}{2|\mathbf{T}_j|} \sum_{k=1}^3 g d_{jk} [B_{jk} - w_j(N_{jk})]^2 \sin(\theta_{jk}) + g(\partial \mathbf{w}_j)_y [\mathbf{B}_j - \bar{\mathbf{w}}_j]. \end{aligned} \quad (3.16)$$

The bed friction term is discretized using the following semi-implicit scheme proposed in [52]:

$$\bar{\mathbf{M}} = \frac{1}{|\mathbf{T}_j|} \int_{\mathbf{T}_j} \mathbf{M}(x, y, t) dx dy = -\frac{gn_f^2}{2} \left(\frac{\sqrt{\bar{q}_{xj}^2 + \bar{q}_{yj}^2}}{\bar{h}_j^{7/3}} \right)^n \begin{bmatrix} 0 \\ \bar{q}_{xj}^n + \bar{q}_{xj}^{n+1} \\ \bar{q}_{yj}^n + \bar{q}_{yj}^{n+1} \end{bmatrix}. \quad (3.17)$$

We use the following desingularization technique to prevent the division by small computed values of water depth:

$$\bar{\mathbf{M}} = -\frac{gn_f^2}{2} \left(\frac{\bar{h}_j^{5/3} \sqrt{\bar{q}_{xj}^2 + \bar{q}_{yj}^2}}{\bar{h}_j^4 + \max\{\bar{h}_j^4, \epsilon\}} \right)^n \begin{bmatrix} 0 \\ \bar{q}_{xj}^n + \bar{q}_{xj}^{n+1} \\ \bar{q}_{yj}^n + \bar{q}_{yj}^{n+1} \end{bmatrix}, \quad (3.18)$$

where we use the same value of ϵ as in Eq. (3.5). The Euler temporal method is applied to discretize the semi-discrete equation of the central-upwind scheme (3.2), which yields to the following explicit expression for the discharge components \bar{q}_{xj}^{n+1} and \bar{q}_{yj}^{n+1} :

$$\begin{aligned} \bar{q}_{xj}^{n+1} &= \frac{\bar{q}_{xj}^n (1 - \Delta t \Phi_j) + \Delta t \Pi_j^{qx} + \Delta t \bar{\mathbf{S}}_j^{(2)}}{1 + \Delta t \Phi_j}, \\ \bar{q}_{yj}^{n+1} &= \frac{\bar{q}_{yj}^n (1 - \Delta t \Phi_j) + \Delta t \Pi_j^{qy} + \Delta t \bar{\mathbf{S}}_j^{(3)}}{1 + \Delta t \Phi_j}, \end{aligned} \quad (3.19)$$

with,

$$\Phi_j = \frac{gn_f^2}{2} \left(\frac{\bar{h}_j^{5/3} \sqrt{\bar{q}_{xj}^2 + \bar{q}_{yj}^2}}{\bar{h}_j^4 + \max\{\bar{h}_j^4, \epsilon\}} \right)^n,$$

and $\Pi_j^{q_x} = \frac{1}{|\mathcal{T}_j|} \sum_{k=1}^3 d_{jk} \mathbf{A}_{jk}^{(2)}$ and $\Pi_j^{q_y} = \frac{1}{|\mathcal{T}_j|} \sum_{k=1}^3 d_{jk} \mathbf{A}_{jk}^{(3)}$ with \mathbf{A}_{jk} are the central-upwind fluxes:

$$\begin{aligned} \mathbf{A}_{jk} = & -\frac{\cos(\theta_{jk})}{b_{jk}^{in} + b_{jk}^{out}} \left[b_{jk}^{in} F(U_{jk}(N_{jk}), B_{jk}) + b_{jk}^{out} F(U_j(N_{jk}), B_{jk}) \right] \\ & -\frac{\sin(\theta_{jk})}{b_{jk}^{in} + b_{jk}^{out}} \left[b_{jk}^{in} G(U_{jk}(N_{jk}), B_{jk}) + b_{jk}^{out} G(U_j(N_{jk}), B_{jk}) \right] \\ & +\frac{b_{jk}^{in} b_{jk}^{out}}{b_{jk}^{in} + b_{jk}^{out}} \left[U_{jk}(N_{jk}) - U_j(N_{jk}) \right]. \end{aligned} \quad (3.20)$$

3.5. Nontrivial well-balanced property

In this section, we prove the nontrivial well-balanced property of the central-upwind scheme (3.2) through the following theorem.

Theorem 3.1. *The numerical scheme (3.2)-(3.17) and the forward Euler time discretization for solving the shallow water equations (2.1)-(2.4) preserves the nontrivial steady-state solutions (2.7).*

Proof 3.2. *We consider a rectangular domain and an inclined topography in the x -direction with $(\partial \mathbf{B}_j)_x = -B_0$ and $(\partial \mathbf{B}_j)_y = 0$, where B_0 is a constant. We assume that at time t^n :*

$$\bar{h}_j^n = h_0 = \left(\frac{n_f^2 q_0^2}{B_0} \right)^{3/10}, \quad \bar{q}_{xj}^n = q_0, \quad \bar{q}_{yj}^n = 0, \quad (3.21)$$

and the following boundary conditions: $u_{jk} = u_j$, $v_{jk} = v_j$ and $h_{jk} = h_j$ in x -direction and $u_{jk} = u_j$, $v_{jk} = 0$ and $h_{jk} = h_j$ in y -direction.

We will prove that $\bar{h}_j^{n+1} = h_0$, $\bar{q}_{xj}^{n+1} = q_0$ and $\bar{q}_{yj}^{n+1} = 0$ at time t^{n+1} . By applying the Euler time discretization to the semi-discrete scheme (3.2), we obtain:

$$\begin{aligned} \bar{\mathbf{U}}_j^{n+1} = & \bar{\mathbf{U}}_j^n - \frac{\Delta t}{|\mathcal{T}_j|} \sum_{k=1}^3 \frac{d_{jk} \cos(\theta_{jk})}{b_{jk}^{in} + b_{jk}^{out}} \left[b_{jk}^{in} F(U_{jk}(N_{jk}), B_{jk}) + b_{jk}^{out} F(U_j(N_{jk}), B_{jk}) \right] \\ & - \frac{\Delta t}{|\mathcal{T}_j|} \sum_{k=1}^3 \frac{d_{jk} \sin(\theta_{jk})}{b_{jk}^{in} + b_{jk}^{out}} \left[b_{jk}^{in} G(U_{jk}(N_{jk}), B_{jk}) + b_{jk}^{out} G(U_j(N_{jk}), B_{jk}) \right] \\ & + \frac{\Delta t}{|\mathcal{T}_j|} \sum_{k=1}^3 \frac{d_{jk} b_{jk}^{in} b_{jk}^{out}}{b_{jk}^{in} + b_{jk}^{out}} \left[U_{jk}(N_{jk}) - U_j(N_{jk}) \right] + \Delta t \bar{\mathbf{S}}_j + \Delta t \bar{\mathbf{M}}_j. \end{aligned} \quad (3.22)$$

The proof is presented in three steps as follows:

-Step 1: Constant water depth. Under the conditions (3.21) the reconstruction (3.8) leads to $h_j = h_{jk} = h_0$, $q_{xj} = q_{xjk} = q_0$ and $q_{yj} = q_{yjk} = 0$ at cell interfaces. Then, the scheme

(3.22) for the continuity equation yields to:

$$\begin{aligned}\bar{\mathbf{w}}_j^{n+1} &= \bar{\mathbf{w}}_j^n - \frac{\Delta t}{|\mathbf{T}_j|} \sum_{k=1}^3 \frac{d_{jk} \cos(\theta_{jk})}{b_{jk}^{in} + b_{jk}^{out}} \left[b_{jk}^{in} q_0 + b_{jk}^{out} q_0 \right] \\ &\quad + \frac{\Delta t}{|\mathbf{T}_j|} \sum_{k=1}^3 \frac{d_{jk} b_{jk}^{in} b_{jk}^{out}}{b_{jk}^{in} + b_{jk}^{out}} \left[w_{jk}(N_{jk}) - w_j(N_{jk}) \right].\end{aligned}\tag{3.23}$$

Since $w = h + B$ and the reconstruction of the bottom topography B is continuous, then $w_{jk}(N_{jk}) - w_j(N_{jk}) = h_{jk}(N_{jk}) - h_j(N_{jk}) = 0$ and Eq. (3.23) reduces to:

$$\begin{aligned}\bar{\mathbf{h}}_j^{n+1} &= \bar{\mathbf{h}}_j^n - \frac{\Delta t}{|\mathbf{T}_j|} \sum_{k=1}^3 \frac{d_{jk} \cos(\theta_{jk})}{b_{jk}^{in} + b_{jk}^{out}} \left[b_{jk}^{in} + b_{jk}^{out} \right] q_0, \\ &= h_0 - \frac{\Delta t}{|\mathbf{T}_j|} \sum_{k=1}^3 d_{jk} \cos(\theta_{jk}) q_0.\end{aligned}\tag{3.24}$$

Thanks to $\sum_{k=1}^3 d_{jk} \cos(\theta_{jk}) = 0$, we have $\bar{\mathbf{h}}_j^{n+1} = h_0$ which shows that the computed water depth remains constant over the domain at time t^{n+1} .

-Step 2: Constant water discharge q_x . Similarly to the water depth, by incorporating the conditions (3.21) in the numerical scheme (3.22) we obtain the following expression for the discharge variable q_x :

$$\begin{aligned}\bar{\mathbf{q}}_{xj}^{n+1} &= q_0 - \frac{\Delta t}{|\mathbf{T}_j|} \sum_{k=1}^3 \frac{d_{jk} \cos(\theta_{jk})}{b_{jk}^{in} + b_{jk}^{out}} \left[b_{jk}^{in} \left(\frac{q_0^2}{h_0} + \frac{1}{2} g h_0^2 \right) + b_{jk}^{out} \left(\frac{q_0^2}{h_0} + \frac{1}{2} g h_0^2 \right) \right] \\ &\quad + \frac{\Delta t g}{2|\mathbf{T}_j|} \sum_{k=1}^3 d_{jk} \cos(\theta_{jk}) h_0^2 - g \Delta t h_0 (\partial \mathbf{w}_j)_x \\ &\quad - \frac{\Delta t g n_f^2 q_0}{2h_0^{7/3}} [q_0 + \bar{\mathbf{q}}_{xj}^{n+1}], \\ &= q_0 - \frac{\Delta t}{|\mathbf{T}_j|} \sum_{k=1}^3 d_{jk} \cos(\theta_{jk}) \left(\frac{q_0^2}{h_0} + \frac{1}{2} g h_0^2 \right) \\ &\quad + \frac{\Delta t g}{2|\mathbf{T}_j|} \sum_{k=1}^3 d_{jk} \cos(\theta_{jk}) h_0^2 - g \Delta t h_0 (\partial \mathbf{w}_j)_x \\ &\quad - \frac{\Delta t g n_f^2 q_0}{2h_0^{7/3}} [q_0 + \bar{\mathbf{q}}_{xj}^{n+1}].\end{aligned}\tag{3.25}$$

Due to $\sum_{k=1}^3 d_{jk} \cos(\theta_{jk}) = 0$ at each cell, we obtain:

$$\bar{\mathbf{q}}_{xj}^{n+1} = q_0 - g \Delta t h_0 (\partial \mathbf{w}_j)_x - \frac{\Delta t g n_f^2 q_0}{2h_0^{7/3}} [q_0 + \bar{\mathbf{q}}_{xj}^{n+1}].\tag{3.26}$$

From the definition of the numerical gradient in Eqs. (3.9)-(3.11), we have $(\partial \mathbf{w}_j)_x = (\partial \mathbf{B}_j)_x = -B_0$. Indeed, recall that the topography is known at the cell vertices and the reconstruction of the topography is linear over each computational cell. Furthermore, in our case the topography is linear over the entire domain, then the following Taylor expansions are exact:

$$\begin{aligned} \mathbf{B}_{j1} &= \mathbf{B}_j + (\partial \mathbf{B}_j)_x(\bar{x}_{j1} - \bar{x}_j) + (\partial \mathbf{B}_j)_y(\bar{y}_{j1} - \bar{y}_j), \\ \mathbf{B}_{j2} &= \mathbf{B}_j + (\partial \mathbf{B}_j)_x(\bar{x}_{j2} - \bar{x}_j) + (\partial \mathbf{B}_j)_y(\bar{y}_{j2} - \bar{y}_j), \\ \mathbf{B}_{j3} &= \mathbf{B}_j + (\partial \mathbf{B}_j)_x(\bar{x}_{j3} - \bar{x}_j) + (\partial \mathbf{B}_j)_y(\bar{y}_{j3} - \bar{y}_j). \end{aligned} \quad (3.27)$$

Since $(\partial \mathbf{B}_j)_y = 0$, then

$$\begin{aligned} \mathbf{B}_{j1} &= \mathbf{B}_j + (\partial \mathbf{B}_j)_x(\bar{x}_{j1} - \bar{x}_j), \\ \mathbf{B}_{j2} &= \mathbf{B}_j + (\partial \mathbf{B}_j)_x(\bar{x}_{j2} - \bar{x}_j), \\ \mathbf{B}_{j3} &= \mathbf{B}_j + (\partial \mathbf{B}_j)_x(\bar{x}_{j3} - \bar{x}_j). \end{aligned} \quad (3.28)$$

According to Eq. (3.10), we have:

$$\begin{aligned} (\partial \mathcal{W}_j)_x &= \frac{(\bar{y}_{j3} - \bar{y}_{j1})(\bar{\mathbf{w}}_{j2} - \bar{\mathbf{w}}_{j1}) - (\bar{y}_{j2} - \bar{y}_{j1})(\bar{\mathbf{w}}_{j3} - \bar{\mathbf{w}}_{j1})}{(\bar{y}_{j3} - \bar{y}_{j1})(\bar{x}_{j2} - \bar{x}_{j1}) - (\bar{y}_{j2} - \bar{y}_{j1})(x_{j3} - x_{j1})}, \\ &= \frac{(\bar{y}_{j3} - \bar{y}_{j1})(\mathbf{B}_{j2} - \mathbf{B}_{j1}) - (\bar{y}_{j2} - \bar{y}_{j1})(\mathbf{B}_{j3} - \mathbf{B}_{j1})}{(\bar{y}_{j3} - \bar{y}_{j1})(\bar{x}_{j2} - \bar{x}_{j1}) - (\bar{y}_{j2} - \bar{y}_{j1})(x_{j3} - x_{j1})}, \\ &= \frac{(\bar{y}_{j3} - \bar{y}_{j1})(\bar{x}_{j2} - \bar{x}_{j1})(\partial \mathbf{B}_j)_x - (\bar{y}_{j2} - \bar{y}_{j1})(\bar{x}_{j3} - \bar{x}_{j1})(\partial \mathbf{B}_j)_x}{(\bar{y}_{j3} - \bar{y}_{j1})(\bar{x}_{j2} - \bar{x}_{j1}) - (\bar{y}_{j2} - \bar{y}_{j1})(x_{j3} - x_{j1})}, \\ &= (\partial \mathbf{B}_j)_x = -B_0, \end{aligned} \quad (3.29)$$

where $(\partial \mathcal{W}_j)_x$ is the first component of the unlimited numerical gradient of the variable w . According to Eq. (3.9), we obtain $(\partial \mathbf{w}_j)_x = (\partial \mathbf{B}_j)_x$. By replacing the numerical gradient $(\partial \mathbf{w}_j)_x$ by $(\partial \mathbf{B}_j)_x = -B_0$ and using $h_0 = (n_f^2 q_0^2 / B_0)^{3/10}$ in Eq. (3.26), we get:

$$\begin{aligned} \bar{q}_{xj}^{n+1} &= \frac{q_0 \left(h_0^{7/3} - \frac{\Delta t g n_f^2}{2} q_0 \right) + \Delta t g B_0 h_0^{10/3}}{h_0^{7/3} + \frac{\Delta t g n_f^2}{2} q_0}, \\ &= \frac{q_0 \left(h_0^{7/3} - \frac{\Delta t g n_f^2}{2} q_0 \right) + \Delta t g n_f^2 q_0^2}{h_0^{7/3} + \frac{\Delta t g n_f^2}{2} q_0}, \\ &= \frac{q_0 \left(h_0^{7/3} + \frac{\Delta t g n_f^2}{2} q_0 \right)}{h_0^{7/3} + \frac{\Delta t g n_f^2}{2} q_0}, \\ &= q_0. \end{aligned} \quad (3.30)$$

This confirms that the computed discharge q_x remains constant over the domain at time t^{n+1} . -Step 3: Zero-water discharge q_y . Here, we will follow the same techniques used for the water discharge q_x to prove that $\bar{\mathbf{q}}_{yj}^{n+1} = 0$. Due to (3.21), the numerical scheme (3.22) for the discharge variable q_y reduces to:

$$\begin{aligned} \bar{\mathbf{q}}_{yj}^{n+1} = & -\frac{\Delta t}{|\mathbf{T}_j|} \sum_{k=1}^3 \frac{d_{jk} \sin(\theta_{jk})}{b_{jk}^{in} + b_{jk}^{out}} \left[\frac{g}{2} h_0^2 (b_{jk}^{in} + b_{jk}^{out}) \right] \\ & + \frac{\Delta t g}{2|\mathbf{T}_j|} \sum_{k=1}^3 d_{jk} \sin(\theta_{jk}) h_0^2 - g \Delta t h_0 (\partial \mathbf{w}_j)_y. \end{aligned} \quad (3.31)$$

Using $\sum_{k=1}^3 d_{jk} \sin(\theta_{jk}) = 0$ at each cell, Eq. (3.31) is simply:

$$\bar{\mathbf{q}}_{yj}^{n+1} = -g \Delta t h_0 (\partial \mathbf{w}_j)_y. \quad (3.32)$$

By incorporating Eq. (3.27) in the second equation of (3.10) and using some straightforward calculations, we obtain $(\mathbf{w}_j)_y = (\mathbf{B}_j)_y = 0$. Then, Eq. (3.32) becomes $\bar{\mathbf{q}}_{yj}^{n+1} = 0$, that is the water discharge in y -direction remains zero over the domain at time t^{n+1} . We conclude that, the numerical scheme (3.2)-(3.17) preserves the nontrivial steady-state solutions.

The same procedure can be applied for the nontrivial steady-state solutions in the y -direction.

4. Numerical experiments

In this section, we perform numerical experiments to investigate the performance of the proposed numerical model for simulating waves propagation and waves run-up on coastal areas. The results of the proposed numerical model are compared with available experimental data from laboratory experiments. In all numerical examples, we used $g = 9.81 \text{ m/s}^2$ for gravity acceleration. We start our numerical experiments by demonstrating the nontrivial well-balanced property of the numerical model in Example 4.1. In Example 4.2, we perform numerical simulations of dam break flow over a sloping bed. In Example 4.3, we simulate the propagation and run-up of breaking and non-breaking solitary waves on a sloping beach. In Example 4.4, we test the ability of the numerical model for simulating periodic waves over a sloping beach. In Example 4.5, we study the evolution of solitary wave over a conical island. Finally in Example 4.6, the proposed numerical model is applied to predict waves propagation along a sloping beach with complex bottom topography.

4.1. Steady flow over a sloping bed

In this first numerical example, we validate the model's ability to preserve nontrivial steady-state solutions over a sloping bed. We consider a computational domain $[0, 2.5] \times [0, 0.2]$ which is discretized using 12863 triangular cells. The bottom topography is as follows:

$$B(x, y) = -0.015(x - 2.53). \quad (4.1)$$

The water depth is initially constant everywhere over the domain $h(x, y, 0) = h_0 = \left(\frac{n_f^2 q_0^2}{0.015}\right)^{3/10}$ with constant flow discharges $q_x(x, y, 0) = q_0$ and $q_y(x, y, 0) = 0$. In our experiments, we study the case for supercritical and subcritical flows. In the supercritical flow case, we use the initial discharge $q_0 = 0.02 \text{ m}^2/\text{s}$ and Manning's coefficient $n = 0.01 \text{ m}^{-1/3}\text{s}$ with Froude number $Fr = 2.058$. While in the subcritical flow case, the initial discharge $q_0 = 0.1 \text{ m}^2/\text{s}$ and Manning's coefficient $n = 0.05 \text{ m}^{-1/3}\text{s}$ are used and Froude number is $Fr = 0.568$. We set the following boundary conditions; $u_{jk} = u_j$, $v_{jk} = v_j$ and $h_{jk} = h_j$ in x -direction and $u_{jk} = u_j$, $v_{jk} = 0$ and $h_{jk} = h_j$ in y -direction.

To assess the accuracy of the numerical model for preserving nontrivial steady-state solutions, we compute errors for L_1 , L_2 and L_∞ norms for water depth h and water discharges q_x and q_y variables at time $t = 150 \text{ s}$ for two case studies shown in Table 1. In Figure 4, we show the computed free-surface elevation and water discharges compared with exact solution at time $t = 150 \text{ s}$. We obtain accurate results and the computed solution remains steady for a large simulation time.

Table 1: Computed errors L_1 , L_2 and L_∞ for the water depth h and water discharges q_x and q_y .

Flow type	Variable	L_1 -error	L_2 -error	L_∞ -error
supercritical	h	7.337×10^{-14}	1.94×10^{-12}	3.1×10^{-15}
	q_x	1.32×10^{-14}	3.20×10^{-13}	5.72×10^{-16}
	q_y	3.85×10^{-18}	4.96×10^{-18}	1.94×10^{-17}
subcritical	h	2.64×10^{-15}	1.93×10^{-13}	1.61×10^{-15}
	q_x	7.51×10^{-14}	3.58×10^{-12}	1.74×10^{-14}
	q_y	1.17×10^{-17}	9.41×10^{-17}	3.22×10^{-16}

4.2. Dam break flow on a sloping bed

In this second numerical example, we consider a laboratory experiment of dam break flow on a sloping bed, carried out by Aureli et al.[54] at Department of Civil Engineering, Parma University. The experiment was conducted on a rectangular flume of 7 m long, 1 m wide, and 0.5 m high with $1 : 10$ sloping bed located at $x = 3.4 \text{ m}$ downstream of the dam as shown in Figure 5. The dam gate was controlled by an oil pressurized circuit located at $x = 2.25 \text{ m}$ [54]. Initially, upstream of the dam, the reservoir has a water depth of 0.25 m while the water depth is zero at the downstream of the dam. In the experiment, complex hydrodynamic behaviors are observed such as run-up and run-down between wet and dry areas. The measurements of the water depth have been performed at four locations G_1 (1.4, 0.5), G_2 (2.25, 0.5), G_3 (3.4, 0.5), and G_4 (4.5, 0.5) along the flume. In the numerical simulations, the computational domain $[0, 7] \times [0, 1]$ is discretized using 18082 triangular cells. The Manning friction coefficient $n_f = 0.01 \text{ m}^{-1/3}\text{s}$ is used, and wall boundary conditions are considered at all sides of the domain except at the outlet side where outflow condition is imposed.

The evolution of the computed water depth using the proposed numerical model and the experimental measurements at the four gauges are shown in Figure 6. Initially, once

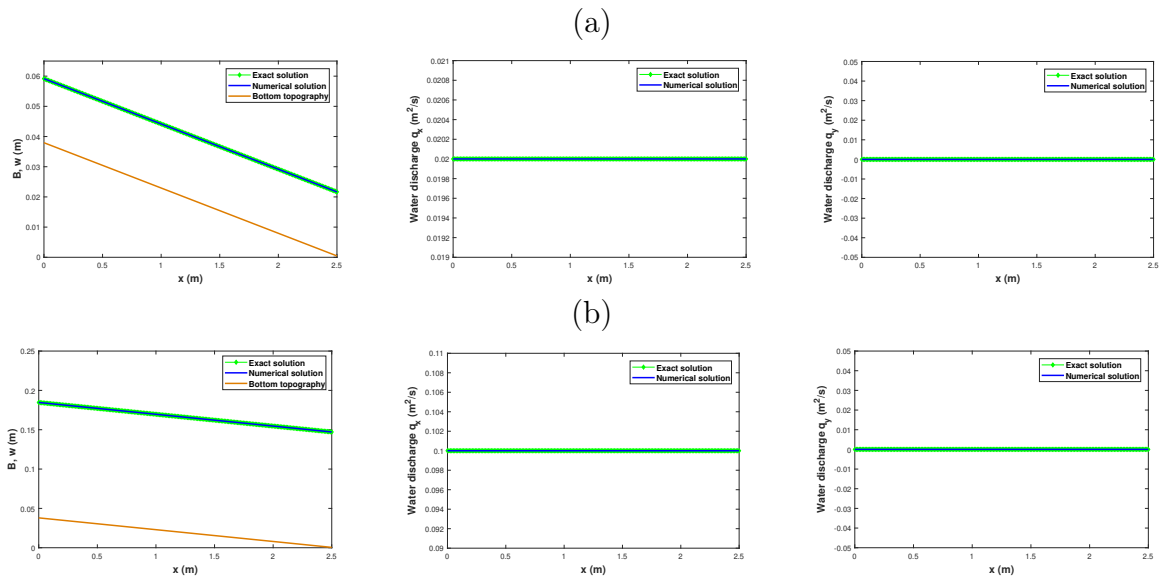


Figure 4: Computed water free-surface elevation and water discharge over a slanted surface at time $t = 150$ s in the supercritical case (a) and in the subcritical case (b).

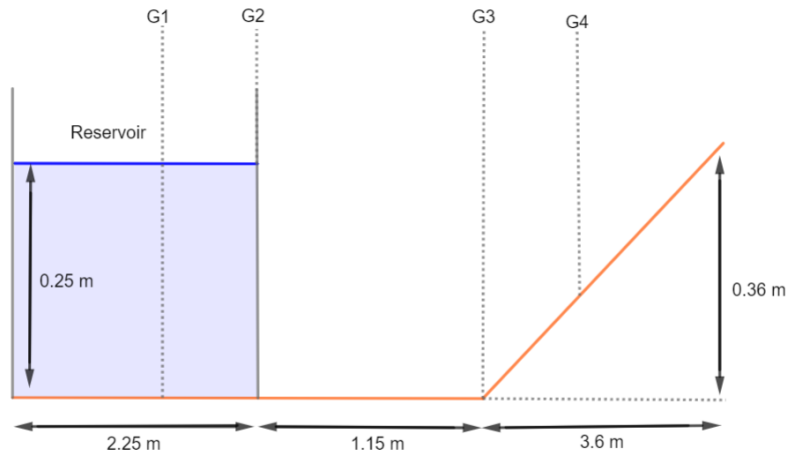


Figure 5: Schematic of the dam-break flow experiment Aureli et al.[54].

the dam gate is removed the water flooded from the reservoir to downstream generating run-up and run-down motions at the sloping bed. The dam-break wave propagates forward and backward over the domain and wave run-up and run-down motions occur several times. Due to the presence of bed friction effects, the flow velocity decreases and the surface water stabilizes for large time. The simulation results show that the time evolution of water depth at the gauges in different locations in space is well predicted compared to experimental measurements which confirms that the proposed numerical model is accurate for modeling waves run-up and run-down between wet and dry zones.

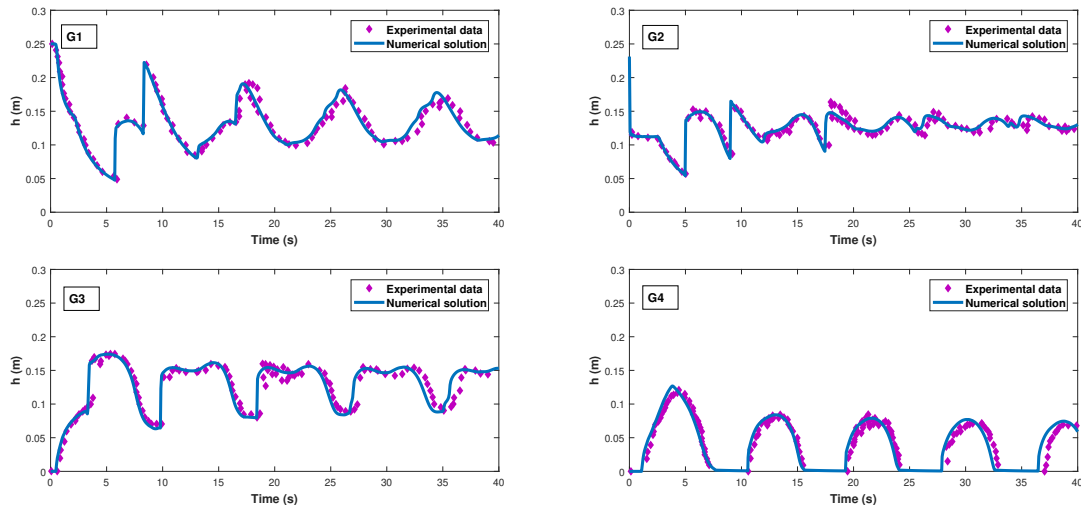


Figure 6: Computed water depth compared with experimental measurements at the four gauges.

4.3. Solitary wave run-up on a sloping beach

In this numerical example, we test the ability of the numerical model for predicting the propagation and run-up of breaking and non-breaking solitary waves on a sloping beach. The numerical results are validated using laboratory experimental data provided by Synolakis [19, 20]. The experiment consists of 1 : 19.85 plane sloping beach of angle φ with constant bed connected to a constant depth region. The initial water surface profile is a solitary wave of height H centered at x_0 which propagates over a still water of constant depth h_0 as shown in Figure 7. In our simulations, we consider the computational domain $[-20, 60] \times [0, 1]$ which is discretized using 41377 triangular cells. The initial condition for free-surface elevation and velocity is [55, 56]:

$$w(x, y, 0) = H \operatorname{sech}^2 \left[\sqrt{\frac{3H}{4h_0^3}} (x - x_0) \right], \quad \mathbf{u}(x, y, 0) = \left[\frac{cw(x, y, 0)}{w(x, y, 0) + h_0}, 0 \right]^T, \quad (4.2)$$

where $c = \sqrt{g(h_0 + H)}$ being the wave velocity. The still water depth $h_0 = 1 \text{ m}$ and the wave height $H = 0.3 \text{ m}$ for breaking and $H = 0.0185 \text{ m}$ for non-breaking waves are used. The Manning friction coefficient is set to $n_f = 0.01 \text{ m}^{-1/3} \text{ s}$ and wall boundary conditions are used at the lateral parts of the computational domain while inflow and outflow conditions are imposed at the right and left boundaries, respectively.

Figure 8 shows the evolution of breaking solitary wave over the sloping beach simulated at different times $t = 0, 1.6, 4.79, 11.18,$ and 17.59 s . The cross section along the x-axis of the computed free-surface elevation is compared with experimental measurements at each time as shown in Figure 8 (left). In Figure 8 (right), we show the three-dimensional view of the computed solution. The wave is initially centered at $x_0 = 14 \text{ m}$ and propagates first over the region of constant depth towards the beach. Once the wave arrives the shoreline,

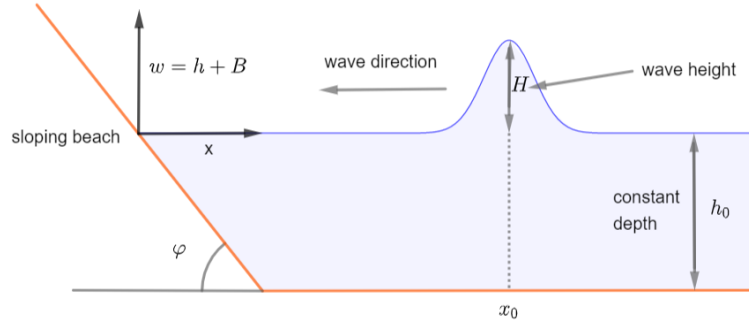


Figure 7: 1D representation of the solitary wave over a sloping beach.

it climbs up the sloping bed to reach its maximum run-up at about time $t = 11.18 s$. The results show that breaking occurs as the wave advances over the region of constant depth, when vertical front of the wave is reached as shown in Figure 8.

For the non-breaking case, the wave is initially centered at $x_0 = 38.5 m$. Figure 9 shows the computed free surface elevation of non-breaking solitary wave at times $t = 8, 11.17, 14.37, 17.56,$ and $20.75 s$, and the results are compared with the experimental measurements. As in the breaking case, the incident wave advances first over the region of constant depth and climbs up the sloping bed when it arrives the shoreline. The wave reaches its maximum run-up at about time $t = 17.56 s$. We observe a good agreement between the numerical simulations and experimental measurements which demonstrates the accuracy of the proposed numerical model for predicting the evolution of breaking and non-braking solitary waves on a sloping beach.

4.4. Periodic waves propagation on a sloping beach

Here, we will assess the ability of the numerical model for predicting the evolution and run-up of periodic waves on a sloping beach, where the numerical results are compared with data from the Cox laboratory experiment [57]. The experiment was conducted in a rectangular flume of 33 m long, 0.6 m wide, and 1.5 m height with $1 : 35$ sloping bed. The periodic waves of height $H = 0.115\text{ m}$ and period $T = 2.2\text{ s}$ were generated at the left boundary of the flume and propagate over a still water of constant depth $h_0 = 0.4\text{ m}$. Measurements for free-surface elevation and velocity were taken at four different locations in space as shown in Figure 10. In our numerical simulations, we consider the computational domain $[0, 8] \times [0, 0.6]$ which is discretized into 15445 triangular cells. The water surface elevation is computed at the locations $L_1 (0, 0.3)$, $L_2 (1.2, 0.3)$, $L_3 (2.4, 0.3)$, and $L_4 (3.6, 0.3)$. We use the set of experimental data for free-surface elevation and velocity at L_1 in our numerical tests as time-varying inflow condition at the left boundary of the domain to generate incoming wave [58, 59, 60]. Wall boundary conditions are considered at the lateral sides and outflow condition is imposed at the right side of the computational domain. The Manning friction coefficient is set to $n_f = 0.01\text{ m}^{-1/3}\text{ s}$.

The time evolution of the computed free-surface elevation and experimental measurements at different locations L_1 , L_2 , L_3 , and L_4 are shown in Figure 11. A good description of the wave distortion with sharpened profile is observed when the wave approaches the bed slope shoreline. The numerical results show that the proposed numerical model is accurate in predicting the evolution of periodic waves on the sloping beach.

4.5. Solitary wave run-up on a conical island

In this numerical example, we further test the accuracy of the proposed numerical model where we consider a laboratory experiment of solitary wave on a conical island. The experiment was carried out by Briggs et al. [61] and it is a simple representation of the Babi island in the Flores Sea in Indonesia. This laboratory experiment was conducted on a basin of 25 m long, 30 m wide with a circular island of base diameter 7.2 m, top diameter 2.2 m, height 0.625 m, and side slope 1 : 4 centered at $\mathbf{x} = (12.98, 13.80)$ as shown in Figure 12. A directional spectral wave-maker was used to generate waves at the left boundary of the basin. In the numerical simulations, the computational domain $[0, 25] \times [0, 30]$ is discretized into 90879 triangular cells. Initially, the water is at rest and incoming solitary waves of height H and constant depth $h_0 = 0.32$ m are generated at the left boundary of the domain, given by [62, 63]:

$$w(t) = H \operatorname{sech}^2 \left[\sqrt{\frac{3H}{4h_0^3}} ct \right], \quad u(t) = \frac{cw(t)}{w(t) + h_0}, \quad (4.3)$$

where we study the case for $H/h_0 = 0.1$ and $H/h_0 = 0.2$ solitary waves. The Manning friction coefficient $n_f = 0.016$ m^{-1/3}s is used, and wall boundary conditions are imposed at the lateral parts while inflow and outflow boundary conditions are respectively used at the left and right sides of the domain. The numerical simulations are performed until the final time $t = 20$ s and the computed free-surface elevation is compared to experimental data at four locations S_1 (9.36, 13.80), S_2 (10.36, 13.8), S_3 (12.96, 11.22), and S_4 (15.56, 13.80) distributed around the island. The predicted and measured free-surface elevation of the solitary waves are presented in Figure 13. We observe a good agreement between the computed numerical solution and laboratory experimental data where the maximum amplitude, arrival time, and phase of the leading waves are well predicted. Furthermore, as emphasized in the previous studies [64, 65, 66], the results show that the breaking appears everywhere around the island for a solitary wave with $H/h_0 = 0.2$ which is characterized by a steeper front as it passes around the conical island. Figure 14 shows the three-dimensional view of the predicted solitary waves profile over the domain at times $t = 4, 6, 8,$ and 10 s. The waves advance first over the domain pushing a large amount of water towards to the conical island. In both two case studies, once the wave arrives the shoreline it climbs up the island to achieve a maximum run-up and then recedes. As expected, when the wave impinges the conical island it reflects and splits into two secondary waves surrounding the island and colliding behind it [64, 65, 66].

4.6. Waves propagation over a complex sloping beach

In this numerical example, we consider a modified test used in [51] to predict the evolution of waves propagating along a sloping beach with complex bottom topography. In our study, we use the bottom topography instead of still water depth [51]. The sloping beach geometry consists of a curved topography connected to a constant depth region [51, 67]. The bottom topography is defined as follows:

$$B(x, y) = \begin{cases} -h_s, & \text{if } x < L_s \\ -h_s + \frac{0.4(x - L_s)}{3 + \cos\left(\frac{\pi y}{L_s}\right)}, & \text{if } x \geq L_s. \end{cases} \quad (4.4)$$

with a sill water depth $h_s = 1.02 \text{ m}$ and a half-wide of the sloping beach $L_s = 8 \text{ m}$. The free-surface elevation is initially constant and incoming wave is generated at the offshore boundary using the following solitary wave [51]:

$$w(t) = \alpha h_s \operatorname{sech}^2 \left[\sqrt{\frac{3g}{4h_s}} \alpha (\alpha + 1) \cdot t \right], \quad (4.5)$$

where $\alpha = H/h_s = 0.2$ with H is the wave height. In our simulations, the computational domain $[0, 30] \times [-8, 8]$ is discretized using 37334 triangular cells. Wall conditions are applied at the side boundaries $y = L_s$ and $y = -L_s$, while inflow and outflow conditions are used at the right $x = 0$ and left $x = 30$ boundaries, respectively. The Manning friction coefficient is set to $n_f = 0.01 \text{ m}^{-1/3}$.

Figure 15 shows the evolution of wave propagating along the sloping beach simulated at different times $t = 0, 2, 4, 6, 8, 10, 11$, and 14 s . The simulation results show that the wave propagates inside the domain from the offshore boundary towards to the shoreline zone generating wave run-up and run-down processes over the sloping bed. Initially, the water is at rest over the domain and at time $t = 0 \text{ s}$, the incoming wave is generated at the offshore boundary of the sloping beach. At time $t = 2 \text{ s}$, the wave advances over the beach pushing a large amount of water towards to the coast. At time $t = 5 \text{ s}$, we observe a wave run-up where the wave starts to climb first the lateral borders and then in the middle of the beach at about time $t = 7 \text{ s}$. The wave recedes from the lateral borders towards the inside the beach while it still propagates and climbs up in the middle of the beach. The wave run-up reaches its maximum in the middle of the beach at about $t = 9 \text{ s}$ and then recedes. Finally, from time $t = 15 \text{ s}$ to $t = 23 \text{ s}$ the wave run-up and run-down motions occur several times and the surface water becomes progressively elongated and steady for long time due to the bed friction effects. The numerical simulations using the proposed numerical model confirm that the model is suitable in the prediction of the propagation of waves along a complex sloping beach.

5. Conclusion

In this study, we proposed a numerical model preserving a class of nontrivial steady-state solutions for predicting waves run-up on coastal areas. In our approach, unstructured central-upwind scheme is used for solving the shallow water flow model over variable bottom topography with bed friction effects. The numerical scheme preserves the stationary steady-states and guarantees the positivity of the water depth. To ensure the accuracy of the numerical model, we used a linear reconstruction for the variables of the system where a positivity correction technique is used for the reconstructed values of the free-surface elevation variable to maintain the non-negativity of the computed water depth. Furthermore, we used a special semi-implicit scheme for the friction source term and a well-balanced formulation for the bottom topography to satisfy the balance between numerical fluxes and source terms at the discrete level. We proved that, the numerical model preserves the nontrivial well-balanced property of steady flow over a slanted surface. The robustness and accuracy of the proposed numerical model are tested performing numerical experiments to simulate waves run-up and run-down processes where the results are compared with laboratory experimental data. The simulation results have shown that the wave profile, the moving shoreline and the waves maximum run-up are well predicted and are in good agreement with experimental data. Finally, the proposed numerical model is validated to predict the evolution of waves propagating along a sloping beach with complex bottom topography.

Acknowledgments

AB gratefully acknowledges funding form UM6P-OCP to support the PhD program of HK.

References

- [1] M. Clare, M. D. Piggott, C. Cotter, Assessing erosion and flood risk in the coastal zone through the application of multilevel monte carlo methods, *Coastal Engineering* 174 (2022) 104118.
- [2] K. Satake, *Tsunamis: case studies and recent developments*, Vol. 23, Springer Science & Business Media, 2005.
- [3] H. S. Ko, P. J. Lynett, A study of long wave run-ups on a bi-linear beach slope induced by solitary and transient-focused wave group, *Coastal Engineering Journal* 61 (2) (2019) 135–151.
- [4] M. Afzal, L. Kumar, Propagation of waves over a rugged topography, *Journal of Ocean Engineering and Science* 7 (1) (2022) 14–28.
- [5] C. Guo, X. Chen, Numerical investigation of large amplitude second mode internal solitary waves over a slope-shelf topography, *Ocean Modelling* 42 (2012) 80–91.
- [6] Z. Xie, T. Stoesser, Two-phase flow simulation of breaking solitary waves over surface-piercing and submerged conical structures, *Ocean Engineering* 213 (2020) 107679.
- [7] D. G., L. F., S. D. A. F., J. F. Filipot, S. S., Wave runup over steep rocky cliffs, *Journal of Geophysical Research: Oceans* 123 (10) (2018) 7185–7205.
- [8] H. von Häfen, C. Krautwald, J. Stolle, D. Bung, N. Goseberg, Overland flow of broken solitary waves over a two-dimensional coastal plane, *Coastal Engineering* 175 (2022) 104125.

- [9] A. Varing, J. Filipot, M. Delpy, G. Guitton, F. Collard, P. Platzner, V. Roeber, D. Morichon, Spatial distribution of wave energy over complex coastal bathymetries: Development of methodologies for comparing modeled wave fields with satellite observations, *Coastal Engineering* 169 (2021) 103793.
- [10] G. Bellotti, A modal decomposition method for the analysis of long waves amplification at coastal areas, *Coastal Engineering* 157 (2020) 103632.
- [11] Y. Wu, P. Higuera, P. Liu, On the evolution and runup of a train of solitary waves on a uniform beach, *Coastal Engineering* 170 (2021) 104015.
- [12] N. Gedik, E. Irtem, M. S. Kabdasli, Experimental investigation on solitary wave run-down and its effects on armor units, *Coastal engineering journal* 48 (4) (2006) 337–353.
- [13] A. Delis, M. Kazolea, N. Kampanis, A robust high-resolution finite volume scheme for the simulation of long waves over complex domains, *International Journal for Numerical Methods in Fluids* 56 (4) (2008) 419–452.
- [14] H. Liu, M. S. Ghidaoui, Z. Huang, Z. Yuan, J. Wang, Numerical investigation of the interactions between solitary waves and pile breakwaters using bkg-based methods, *Computers & Mathematics with Applications* 61 (12) (2011) 3668–3677.
- [15] H. Zhu, L. Wang, E. Avital, H. Tang, J. Williams, Numerical simulation of shoaling broad-crested internal solitary waves, *Journal of Hydraulic Engineering* 143 (6) (2017) 04017006.
- [16] J. Domínguez, C. Altomare, J. Gonzalez-Cao, P. Lomonaco, Towards a more complete tool for coastal engineering: solitary wave generation, propagation and breaking in an sph-based model, *Coastal Engineering Journal* 61 (1) (2019) 15–40.
- [17] A. Farhadi, H. Emdad, E. G. Rad, On the numerical simulation of the nonbreaking solitary waves run up on sloping beaches, *Computers & Mathematics with Applications* 70 (9) (2015) 2270–2281.
- [18] N. Dodd, Numerical model of wave run-up, overtopping, and regeneration, *Journal of Waterway, Port, Coastal, and Ocean Engineering* 124 (2) (1998) 73–81.
- [19] C. Synolakis, The runup of long waves [dissertation], Pasadena, CA: California Institute of Technology (1986).
- [20] C. E. Synolakis, The runup of solitary waves, *Journal of Fluid Mechanics* 185 (1987) 523–545.
- [21] O. S. Madsen, C. C. Mei, The transformation of a solitary wave over an uneven bottom, *Journal of Fluid Mechanics* 39 (4) (1969) 781–791.
- [22] K. Kaplan, Generalized laboratory study of tsunami run-up, no. 60, US Beach Erosion Board, 1955.
- [23] B. De St Venant, Theorie du mouvement non-permanent des eaux avec application aux crues des rivières et à l'introduction des marées dans leur lit, *Académie de Sci. Comptes Rendus* 73 (99) (1871) 148–154.
- [24] P. García-Navarro, J. Murillo, J. Fernández-Pato, I. Echeverribar, M. Morales-Hernández, The shallow water equations and their application to realistic cases, *Environmental Fluid Mechanics* 19 (5) (2019) 1235–1252.
- [25] G. Hernandez-Duenas, A. Beljadid, A central-upwind scheme with artificial viscosity for shallow-water flows in channels, *Advances in Water Resources* 96 (2016) 323–338.
- [26] A. Beljadid, A. Mohammadian, H. Qiblawey, Numerical simulation of rotation dominated linear shallow water flows using finite volume methods and fourth order adams scheme, *Computers & fluids* 62 (2012) 64–70.
- [27] A. Beljadid, A. Mohammadian, H. M. Qiblawey, An unstructured finite volume method for large-scale shallow flows using the fourth-order adams scheme, *Computers & Fluids* 88 (2013) 579–589.
- [28] D. O., D. F., J. F., L. C. L. C. C. S., Fullswof: Full shallow-water equations for overland flow, *Journal of Open Source Software* 2 (20) (2017) 448.
- [29] M. Ricchiuto, A. Bollermann, Stabilized residual distribution for shallow water simulations, *Journal of Computational Physics* 228 (4) (2009) 1071–1115.
- [30] H. Karjoun, A. Beljadid, Modelling of coupled surface and subsurface water flows, in: *Canadian Society of Civil Engineering Annual Conference*, Springer, 2022, pp. 589–601.
- [31] V. V. Titov, C. E. Synolakis, Modeling of breaking and nonbreaking long-wave evolution and runup using vtcs-2, *Journal of Waterway, Port, Coastal, and Ocean Engineering* 121 (6) (1995) 308–316.
- [32] K. Hu, C. Mingham, D. M. Causon, Numerical simulation of wave overtopping of coastal structures

- using the non-linear shallow water equations, *Coastal engineering* 41 (4) (2000) 433–465.
- [33] M. Brocchini, N. Dodd, Nonlinear shallow water equation modeling for coastal engineering, *Journal of waterway, port, coastal, and ocean engineering* 134 (2) (2008) 104–120.
 - [34] S. Liang, T. Hsu, Least-squares finite-element method for shallow-water equations with source terms, *Acta Mechanica Sinica* 25 (5) (2009) 597–610.
 - [35] R. J. LeVeque, *Finite volume methods for hyperbolic problems*, Vol. 31, Cambridge university press, 2002.
 - [36] Q. Liang, F. Marche, Numerical resolution of well-balanced shallow water equations with complex source terms, *Advances in water resources* 32 (6) (2009) 873–884.
 - [37] D. George, Augmented riemann solvers for the shallow water equations over variable topography with steady states and inundation, *Journal of Computational Physics* 227 (6) (2008) 3089–3113.
 - [38] J. Zhou, D. M. Causon, D. Ingram, C. Mingham, Numerical solutions of the shallow water equations with discontinuous bed topography, *International journal for numerical methods in fluids* 38 (8) (2002) 769–788.
 - [39] C. L. Mader, *Numerical modeling of water waves*, CRC press, 2004.
 - [40] A. Kurganov, S. Noelle, G. Petrova, Semidiscrete central-upwind schemes for hyperbolic conservation laws and hamilton–jacobi equations, *SIAM Journal on Scientific Computing* 23 (3) (2001) 707–740.
 - [41] A. Kurganov, G. Petrova, Central-upwind schemes on triangular grids for hyperbolic systems of conservation laws, *Numerical Methods for Partial Differential Equations: An International Journal* 21 (3) (2005) 536–552.
 - [42] A. Kurganov, D. Levy, Central-upwind schemes for the saint-venant system, *ESAIM: Mathematical Modelling and Numerical Analysis* 36 (3) (2002) 397–425.
 - [43] A. Beljadid, A. Mohammadian, A. Kurganov, Well-balanced positivity preserving cell-vertex central-upwind scheme for shallow water flows, *Computers & Fluids* 136 (2016) 193–206.
 - [44] X. Liu, A. Beljadid, A coupled numerical model for water flow, sediment transport and bed erosion, *Computers & Fluids* 154 (2017) 273–284.
 - [45] A. Beljadid, P. LeFloch, A central-upwind geometry-preserving method for hyperbolic conservation laws on the sphere, *Communications in Applied Mathematics and Computational Science* 12 (1) (2017) 81–107.
 - [46] H. Shirkhani, A. Mohammadian, O. Seidou, A. Kurganov, A well-balanced positivity-preserving central-upwind scheme for shallow water equations on unstructured quadrilateral grids, *Computers & Fluids* 126 (2016) 25–40.
 - [47] A. Hanini, A. Beljadid, D. Ouazar, A well-balanced positivity-preserving numerical scheme for shallow water models with variable density, *Computers & Fluids* 231 (2021) 105156.
 - [48] A. Kurganov, G. Petrova, A second-order well-balanced positivity preserving central-upwind scheme for the saint-venant system, *Commun. Math. Sci.* 5 (1) (2007) 133–160.
 - [49] A. Chertock, S. Cui, A. Kurganov, T. Wu, Well-balanced positivity preserving central-upwind scheme for the shallow water system with friction terms, *International Journal for numerical methods in fluids* 78 (6) (2015) 355–383.
 - [50] S. Bryson, Y. Epshteyn, A. Kurganov, G. Petrova, Well-balanced positivity preserving central-upwind scheme on triangular grids for the saint-venant system, *ESAIM: Mathematical Modelling and Numerical Analysis* 45 (3) (2011) 423–446.
 - [51] M. Brocchini, R. Bernetti, A. Mancinelli, G. Albertini, An efficient solver for nearshore flows based on the waf method, *Coastal Engineering* 43 (2) (2001) 105–129.
 - [52] H. Karjoun, A. Beljadid, P. G. LeFloch, A structure-preserving algorithm for surface water flows with transport processes, *Advances in Computational Mathematics* 48 (1) (2022) 1–32.
 - [53] P. Jawahar, H. Kamath, A high-resolution procedure for euler and navier–stokes computations on unstructured grids, *Journal of Computational Physics* 164 (1) (2000) 165–203.
 - [54] F. Aureli, P. Mignosa, M. Tomirotti, Numerical simulation and experimental verification of dam-break flows with shocks, *Journal of hydraulic research* 38 (3) (2000) 197–206.
 - [55] Y. Que, K. Xu, The numerical study of roll-waves in inclined open channels and solitary wave run-up,

- International journal for numerical methods in fluids 50 (9) (2006) 1003–1027.
- [56] A. Mahdavi, N. Talebbeydokhti, Modeling of non-breaking and breaking solitary wave run-up using force-muscl scheme, *Journal of Hydraulic Research* 47 (4) (2009) 476–485.
 - [57] D. Cox, Experimental and numerical modeling of surf zone hydrodynamics. phd thesis, Ph.D. thesis, University of Delaware (1995).
 - [58] A. Duran, F. Marche, Recent advances on the discontinuous galerkin method for shallow water equations with topography source terms, *Computers & Fluids* 101 (2014) 88–104.
 - [59] P. Bonneton, Dynamique non linéaire des vagues en zone de surf interne, *Revue française de génie civil* 7 (9) (2003) 1061–1076.
 - [60] F. Marche, Theoretical and numerical study of shallow water models: applications to nearshore hydrodynamics. phd thesis, Ph.D. thesis, Bordeaux 1 (2005).
 - [61] M. J. Briggs, C. E. Synolakis, G. S. Harkins, D. R. Green, Laboratory experiments of tsunami runup on a circular island, *Pure and applied geophysics* 144 (3) (1995) 569–593.
 - [62] I. K. Nikolos, A. I. Delis, An unstructured node-centered finite volume scheme for shallow water flows with wet/dry fronts over complex topography, *Computer Methods in Applied Mechanics and Engineering* 198 (47-48) (2009) 3723–3750.
 - [63] S. Bradford, B. Sanders, Finite-volume model for shallow-water flooding of arbitrary topography, *Journal of hydraulic engineering* 128 (3) (2002) 289–298.
 - [64] P. Liu, Y. Cho, M. J. Briggs, U. Kanoglu, C. E. Synolakis, Runup of solitary waves on a circular island, *Journal of Fluid Mechanics* 302 (1995) 259–285.
 - [65] Y. Yamazaki, Z. Kowalik, K. Cheung, Depth-integrated, non-hydrostatic model for wave breaking and run-up, *International journal for numerical methods in fluids* 61 (5) (2009) 473–497.
 - [66] Y. Wei, X. Mao, K. Cheung, Well-balanced finite-volume model for long-wave runup, *Journal of Waterway, Port, Coastal, and Ocean Engineering* 132 (2) (2006) 114–124.
 - [67] H. T. Özkan-Haller, J. T. Kirby, A fourier-chebyshev collocation method for the shallow water equations including shoreline runup, *Applied Ocean Research* 19 (1) (1997) 21–34.

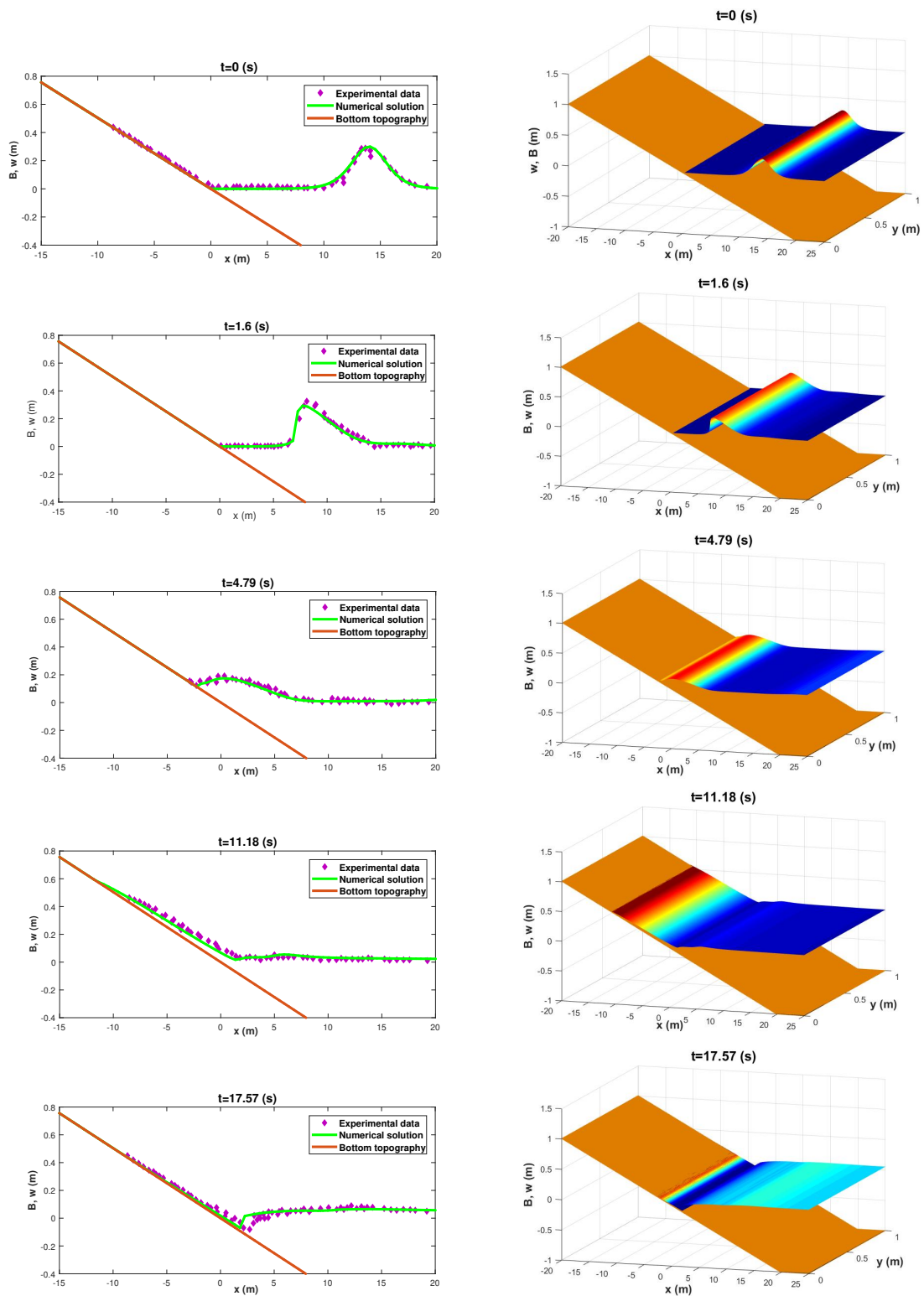


Figure 8: Modeling of breaking solitary wave on a sloping beach: Predicted free-surface elevation compared with experimental measurements at different times (left) and the corresponding three-dimensional view (right).

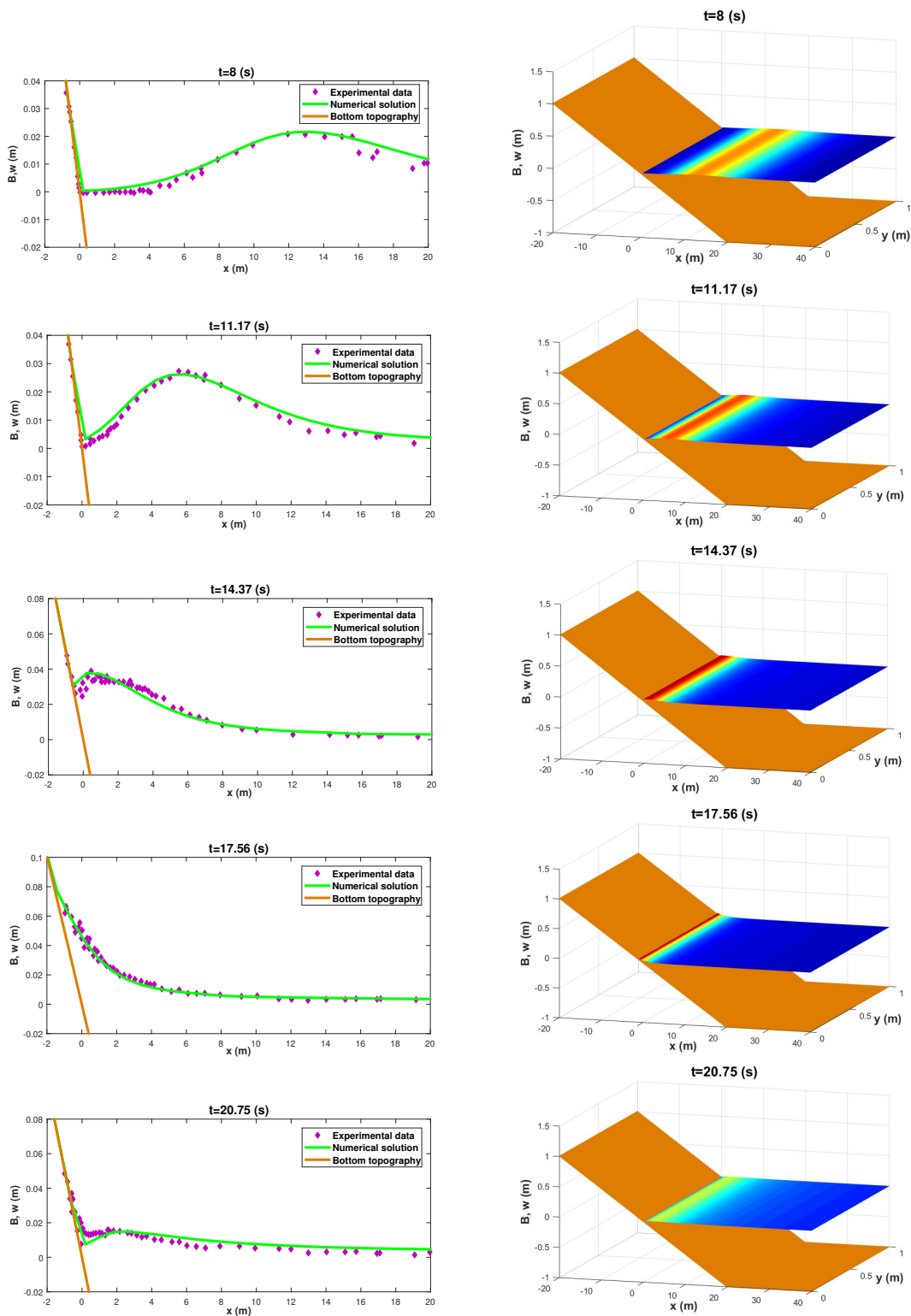


Figure 9: Modeling of non-breaking solitary wave over a sloping beach: Predicted free surface elevation compared to experimental measurements at different times (left) and the corresponding three-dimensional view (right).

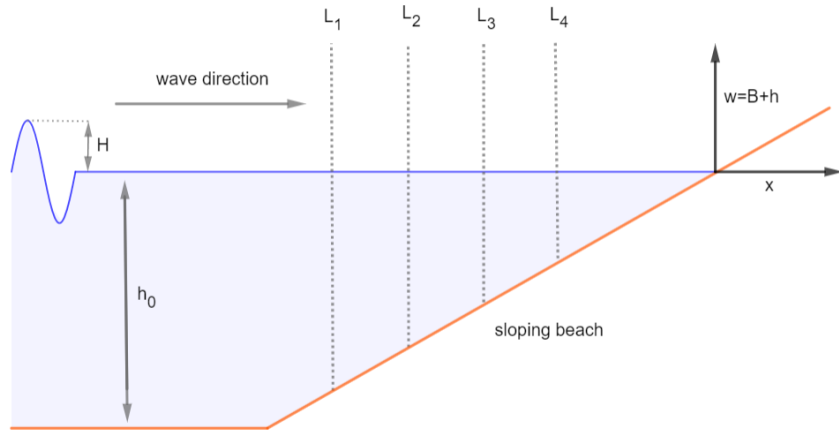


Figure 10: A sketch of periodic wave propagation on a sloping beach.

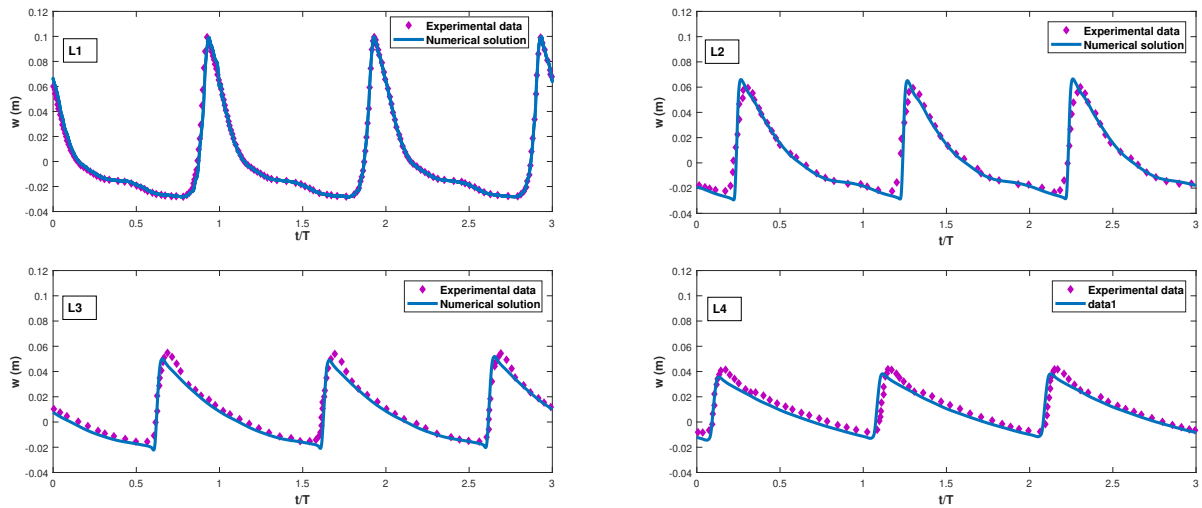


Figure 11: The time evolution of simulated and measured free-surface elevation at the four locations.

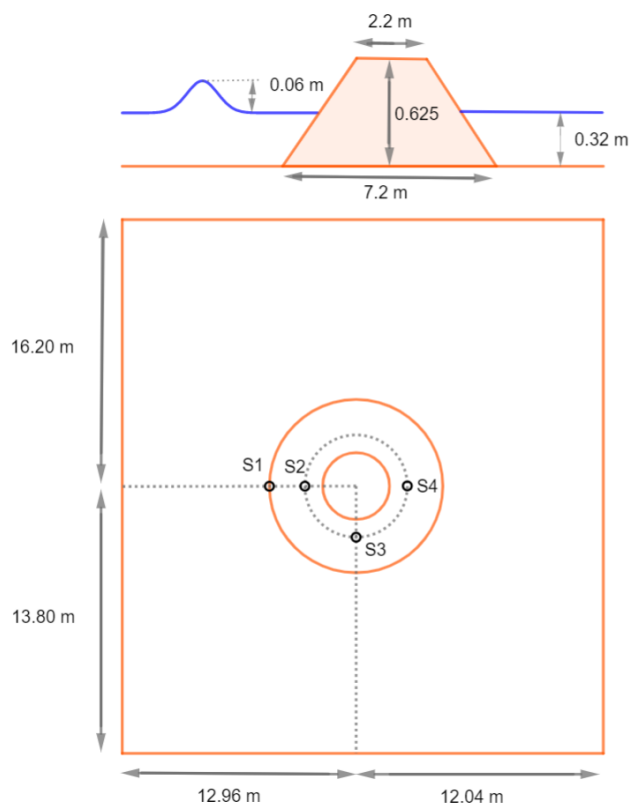


Figure 12: A sketch for the solitary wave on a conical island.

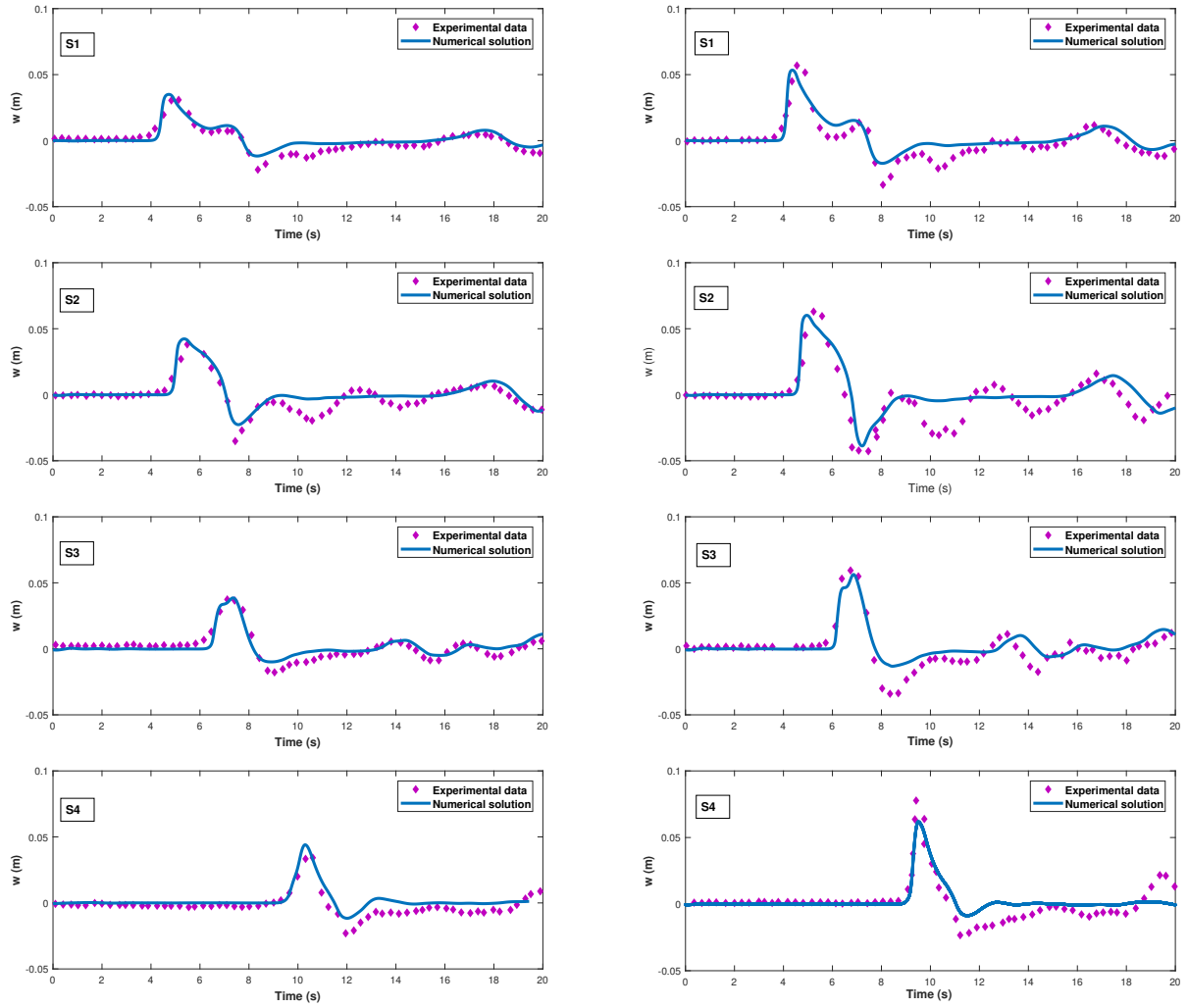


Figure 13: The time evolution of the free-surface elevation computed at the four gauges: Numerical solution compared with experimental measurements for $H/h_0 = 0.1$ (left) and $H/h_0 = 0.2$ (right) solitary waves.

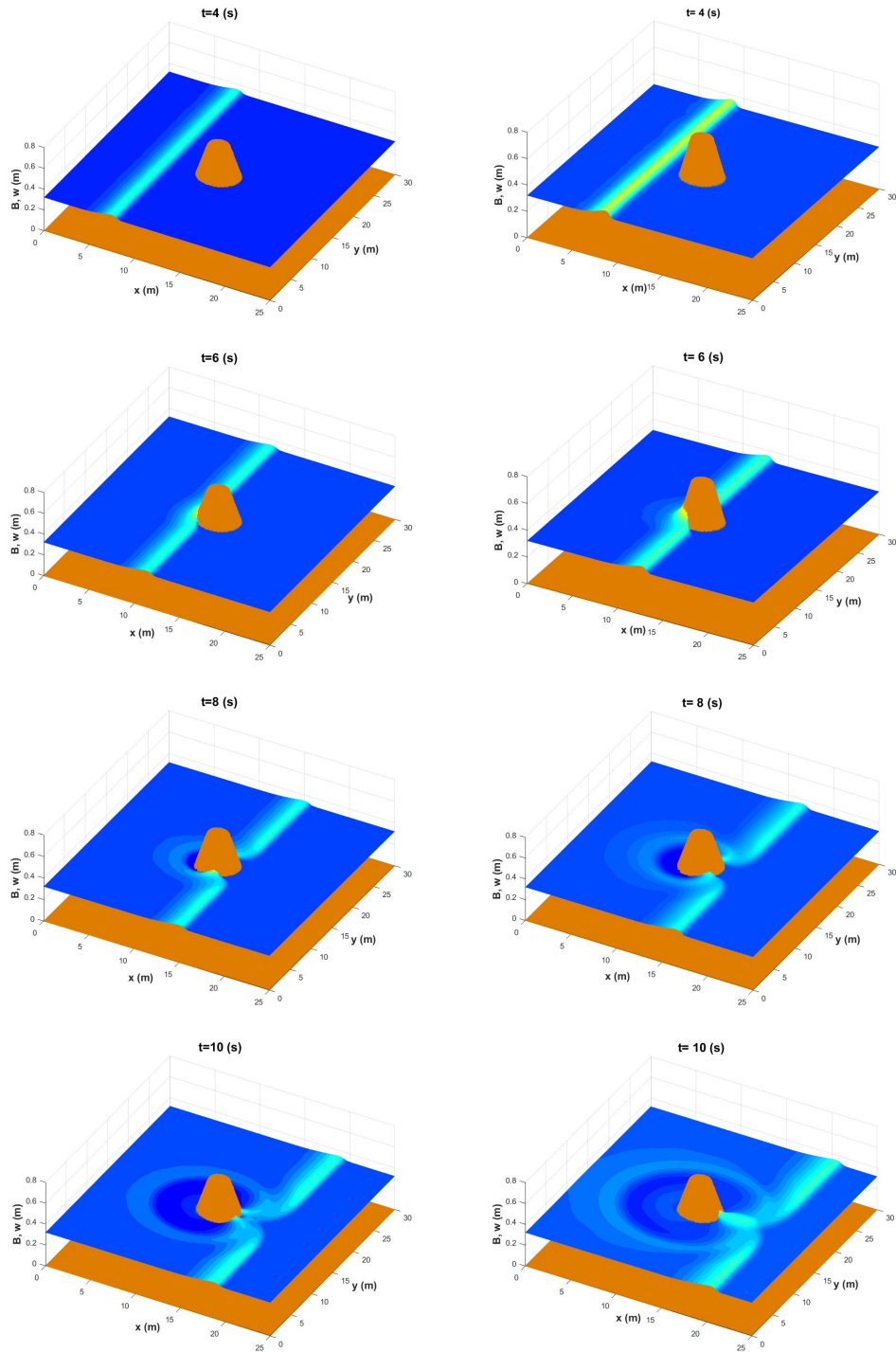


Figure 14: Modeling of solitary waves for $H/h_0 = 0.1$ (left) and $H/h_0 = 0.2$ (right) over the conical island: Three-dimensional view of the computed free-surface elevation at times $t = 4, t = 6, t = 8$, and $t = 10$ s.

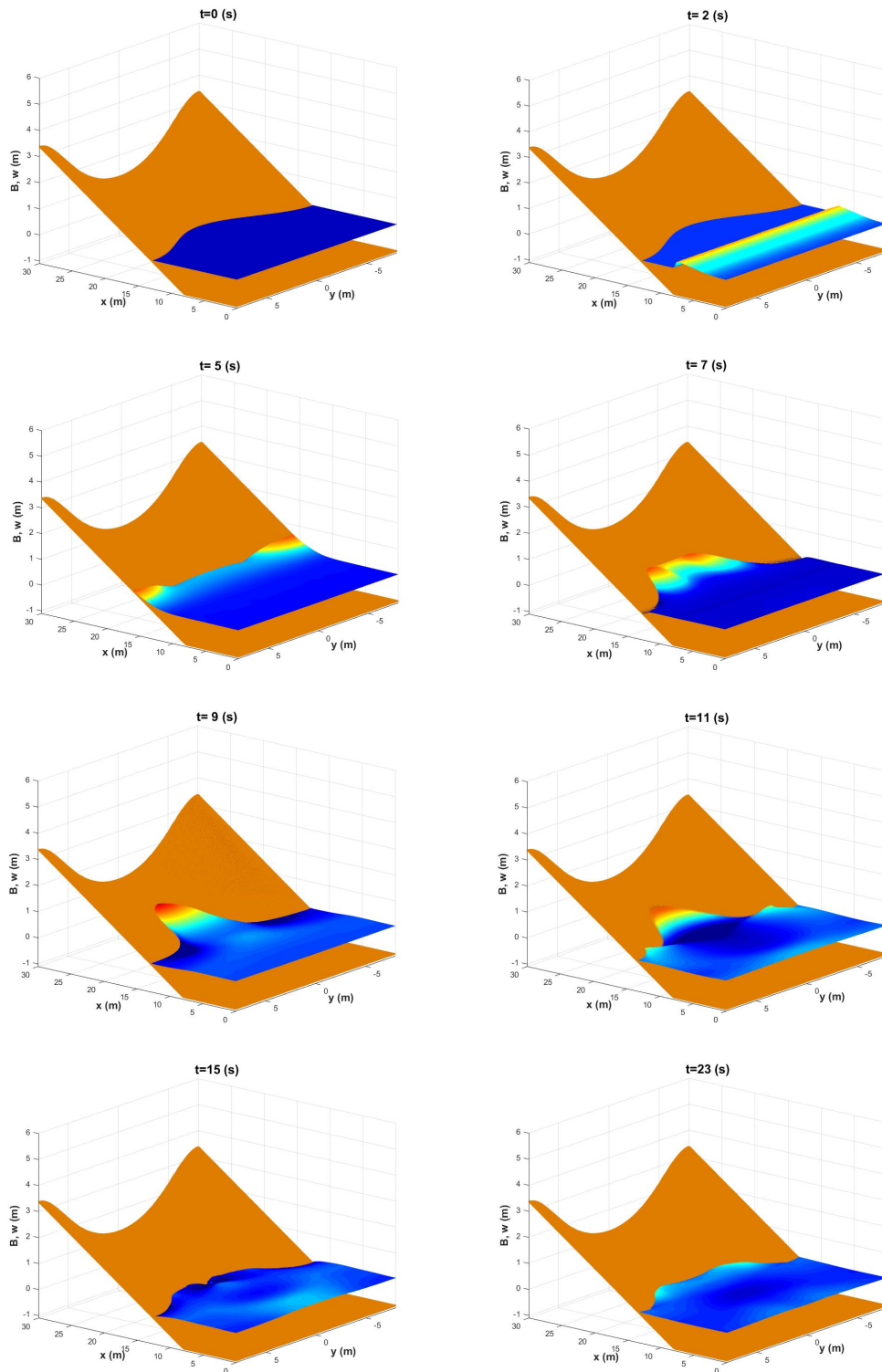


Figure 15: Modeling of solitary wave over a sloping beach with complex topography: Three-dimensional view of the wave propagation along the beach at different times.